# Nanostructured Non-precious Oxygen Reduction Reaction Catalysts for Electrochemical Energy Applications

by

Jason Wu

A thesis

presented to the University of Waterloo

in fulfillment of the

thesis requirement for the degree of

Master of Applied Science

in

Chemical Engineering

Waterloo, Ontario, Canada, 2015

© Jason Wu 2015

# Author's declaration

I hereby declare that I am the sole author of this thesis. This is a true copy of my thesis, including any required final revisions as accepted by my examiners.

I understand that my thesis may be made electronically available to the public.

# Abstract

Fuel cell and state of the art battery technologies share a common electrochemical reaction in their operation. The oxygen reduction reaction (ORR) is a key phenomenon for the efficient operation for both electrochemical devices. However, ORR often suffers from slow kinetics and requires electrocatalysts to increase the kinetics of the reaction to practical levels. The use of platinum based catalysts has long been considered the most effective solution in improving ORR kinetics; however, platinum is an extremely expensive metal and is limited in world supply. It is critical to find alternative, non-precious catalysts to replace platinum catalysts. Heat treated non-precious catalysts produced through high temperature pyrolysis of temperatures over 600°C are promising class of materials, showing high catalytic activity and stability in both acidic and alkaline conditions. However, heat treated non-precious catalysts do not match platinum based catalysts in terms of stability and activity. Furthermore, the active sites of heat treated non-precious catalysts are still under debate. In the present work, non-precious carbon catalysts were synthesized via pyrolysis of carbon in the presence of nitrogen and a transition metal then evaluated and characterized. Iron is chosen as the transition metal for all of the experiments as it is naturally abundant, relatively safe, and displays the highest activity amongst transition metals in this application. In fact, iron displays the highest redox potential which has been noted to be related to the binding of dioxygen species. A number of different catalysts were synthesized then studied by varying the synthesis conditions and precursors employed to increase the activity of non-precious carbon catalysts. First, a new nitrogen rich ligand is synthesized to be used as the nitrogen source during pyrolysis. This ligand will chelate with iron in the system and thus will help prevent agglomeration of iron particles during pyrolysis, resulting in many isolated active sites. The ratios of iron to ligand were varied and the

affects of varying the mass of iron in the system on catalytic activity was studied. Following this work, support-less catalysts focusing on employing one-dimensional nanofiber structures were synthesized using polyacrylonitrile as the basis of producing one-dimensional nanofibers. One-dimensional nanofibrous electrocatalysts were synthesized via electrospinning a solution of polyacrylonitrile in DMF. Iron was added into the solution as well to ensure the electrospun fibers were well impregnated with iron. The resulting nanofibers were then pyrolyzed and the catalysts were evaluated and characterized. The results that followed indicated that surface area and porosity of catalysts plays a significant role in obtaining highly active catalysts. Highly porous carbon catalysts were then synthesized, evaluated, and characterized as a result of this discovery. These catalysts were produced via electrospinning an emulsion of polyacrylonitrile and fumed silica particles. After pyrolysis, these particles were removed by treating the catalyst with HF acid. The results of the work completed have shown that it is possible to produce non-precious catalysts that can replace platinum, bringing us a step closer to full commercialization of renewable energy devices.

# Acknowledgement

The present work was financially supported by the University of Waterloo.

The author would like to thank Dr. Zhongwei Chen and Dr. Aiping Yu for their continued assistance throughout the author's study.

The author would also like to give special thanks to his colleagues including, but not limited to, Drew Higgins Ja-Yeon Choi, Zhu Chen, Dr. Wenmu Li, Gaopung Jiang, Hadis Zarrin, Kun Feng, Abdul Ghannou, and Dong-Un Lee.

Lastly, the author appreciates the time and critical input given by the reviewers of this thesis: Dr. Zhongwei Chen, Dr. Aiping Yu, and Dr. Michael Fowler.

# Table of Contents

# List of Figures

# List of Tables

# List of abbreviations and terms

| | |
|---|---|
| **ORR** | Oxygen reduction reaction |
| **TPPQ** | 2,3,7,8-Tetra(pyridin-2-yl)pyrazino[2,3-g]quinoxaline |
| **PAN** | Polyacrylonitrile |
| **Pt/C** | Platinum on carbon catalyst |
| **RDE** | Rotating disk electrode |
| **RRDE** | Rotating ring disk electrode |
| **Pc** | Phthalocyanine |
| **Py** | Pyrrole |
| **Ppy** | Polypyrrole |
| **Fe** | Iron |
| **SEM** | Scanning electron microscopy |
| **TEM** | Transmission electron microscopy |
| **BET** | Brunner Emmett Teller |
| **XPS** | X-ray photoemission spectroscopy |
| **XRD** | X-ray diffraction |
| **CV** | Cyclic Voltammetry |
| **LSV** | Linear sweep voltammetry |
| **$HClO_4$** | Perchloric acid |
| **KOH** | Potassium hydroxide |
| **HF** | Hydrofluoric acid |
| **$SiO_2$** | Silicon Dioxide |
| **PEMFC** | Polymer electrolyte membrane fuel cell or proton exchange membrane fuel cell |
| **SOFC** | Solid oxide fuel cell |

| | |
|---|---|
| **MCFC** | Molten carbonate fuel cell |
| **AFC** | Alkali fuel cell |
| **PAFC** | Phosphoric acid fuel cell |
| **M-N/C** | Metal-Nitrogen/Carbon type of pyrolyzed catalysts |
| **NPMC** | Non-precious metal catalyst |

# 1. Introduction

## 1.1 Scope and Objective

The population of the world as of the year 2013 reached a population of roughly 7.1 billion people and continues to rise at an annual basis. The rise in world population sees a rise in demand for the production of goods and services, all of which results in higher demand for energy. Currently, the combustion of fossil fuels is a major source of energy for high energy demand applications, providing power to be supplied by power plants and powering automobiles. However, in addition to potential harmful effects as a result of the burning of fossil fuels, fossil fuels are not limitless and will continue to be consumed at increasing rates according to increasing demand for energy. To maintain the current quality of living and maintain a sustainable environment, it is critical to research and develop clean and renewable sources of energy and power generation.

Electrochemical devices such as fuel cells and batteries have been known to provide clean, efficient, and direct conversion of reactants into electricity. Proton Exchange Membrane or Polymer Electrolyte Membrane (PEM) fuel cells are a proven technology for providing clean and efficient energy.[1-4] PEM fuel cells can be used in a variety of applications, including the power stations, portable devices, and electric vehicles. Batteries as well have long been used in many portable devices, with the most recent lithium-ion battery technology even used in automotive vehicles. The current state of battery technology has been proven to work in electric vehicles; however, the energy density provided by current lithium-ion batteries still pales in

comparison to the combustion engine.[5,6] It is impossible to operate a vehicle for the same length of time provided by the burning of fossil fuels, given the currently commercially available battery technology. Metal-air batteries are a new development in battery technology that replaces its cathode with an air-breathing electrode, employing the reduction of oxygen as its cathodic half-cell reaction.[5,6] Fuel cells operate on the same principle where oxygen is reduced at the cathode as the associated half-cell reaction to the generation of electrons produced at the anode.[1,2,4,7] Both PEM fuel cell and metal-air battery technologies rely on the oxygen reduction reaction (ORR), which is notorious for its extremely slow kinetics. For PEM fuel cells and metal-air batteries to be usable and practical, electrocatalysts that are active towards ORR must be used to speed up the electrochemical reaction.

As of now, platinum based catalysts are the only commercially available catalysts for ORR, and due to their high activity and stability in both aqueous acidic and alkaline environments is an extremely attractive solution to catalyze ORR to a practical and usable level. However, platinum is an extremely expensive metal and known to be limited in world supply. Although both electrochemical devices benefit greatly from increased ORR kinetics due to the use of platinum based catalysts, the increase in cost in the production of the electrochemical devices due to the use of platinum is a significant deterrent in the commercialization and widespread use of PEM fuel cells or metal-air batteries. Maintaining low costs is often the key in the universal adoption of a technology, and the use of platinum based catalysts is in direct conflict with this principle. Two approaches have been proposed to rectify the issue regarding the high cost of platinum: (1) increase the utilization or effectiveness of platinum catalysts, so less platinum need to be used, or (2) completely replace platinum catalysts with non-precious

alternatives.[1] In the long term, it is far more desirable to take the second approach and completely replace platinum with non-precious metal catalysts as the first approach does not address the issue of limited world supply of platinum.

The development of low cost of highly active ORR catalysts consisting of abundantly found materials will greatly benefit the commercialization of PEM fuel cell and metal-air battery technologies. A common approach to developing low cost active ORR catalysts is the use of high surface area carbon along with a transition metal and nitrogen pore filler.[1,2,8-21] Pyrolysis of the carbon/transition metal/nitrogen precursor results in active ORR catalysts exhibiting high stability in both alkaline and acidic conditions. A second approach is to synthesize transition metal macrocyclic molecules[1,2,7,22-29] which are known to possess catalytic activity towards ORR. However, these macrocycles are not stable in acidic conditions without adjusting the molecular structure of the macrocycle.[27] The main goal of this research is the development of highly active nanostructured non-precious ORR catalysts for both acidic and alkaline conditions.

The focus of this research is to investigate potential active non-precious catalysts for the oxygen reduction reaction to be used in electrochemical PEM fuel cells or Metal-air batteries. The research focuses on a class of carbon based non-precious electrocatalysts synthesizd via high temperature pyrolysis of carbon and a transition metal salt. The presence of nitrogen is also deemed necessary and is introduced via two different methods as will be discussed. Synthesized catalysts are evaluated for their catalytic activity in both acidic and basic conditions, signifying applications in both PEM fuel cells and Metal-air batteries. Specifically, three types of catalysts are synthesized and investigated using organic ligands containing high nitrogen content; (1)

TPPQ in carbon black, (2) electrospun PAN, and (3) electrospun PAN with sacrificial silica particles.

The research investigates a number of morphologies, including high surface area carbon black, one-dimensional structures, and porous structures, and their effects on the ORR activity of non-precious catalysts. The non-precious catalysts are low in cost and make use of readily available materials. Furthermore, due to the structure of the catalysts, the catalysts do not require a support. The one-dimensional structures of catalysts are investigated due to potential benefits such as improved conductivity provided by better contact between the nanofibrous catalysts, improved stability, and increased surface area.[30] Lastly, a highly porous structured catalyst allows for the formation of more ORR active sites,[31] and facilitates diffusion of reactants and the results of such are investigated.

## 1.2 Contents of the thesis

Chapter 2 of the thesis contains a brief description of the electrochemical energy devices (PEM Fuel cell and Meta-air battery) that involve the oxygen reduction reaction. The role of oxygen reduction reaction in the electrochemical devices is also discussed. A brief review regarding non-precious oxygen reduction reaction is conducted, including proposed mechanisms in both acidic and alkaline conditions. Chapter 3 of the thesis introduces the common synthesis techniques and characterization methods in synthesizing and characterizing the non-precious catalysts. Chapter 3 also discusses the methods and techniques used to evaluate the efficacy of the catalyst and includes a look at the materials used. Chapter 4 of the thesis discusses and explores the results of the research and discusses the lessons learned from the work completed.

The chapter mainly discusses two published works regarding heat treated non-precious catalysts. The first work, a preliminary study regarding heat treated catalysts, discusses current issues regarding heat treated non-precious catalysts and an approach to rectify a specific issue. This issue involves the formation of large iron particles during high temperature pyrolysis that negative effects the activity of the catalyst. To combat this issue, a nitrogen-rich ligand was designed and synthesized to be used as a high surface area carbon pore filler for high temperature pyrolysis. The second work looks at employing electrospinning techniques to create nanofibrous non-precious catalysts which are produced after pyrolysis. These nanofibers are spun along with a transition metal precursor with polyacrylonitrile as the fibrous polymer. Polyacrylonitrile is an excellent material to be used for catalyst synthesis of this kind as it is rich in nitrogen and is stable during the high temperature pyrolysis. Based on what was learned from the working with polyacrylonitrile fibrous catalysts, a third section discusses a method to improve the catalytically activity by improving the physical characteristics of the catalyst. This is done so by introducing sacrificial silica particles into the electrospinning solution and removing the silica particles after pyrolysis to introduce voids into the fibers. Lastly, Chapter 5 summarizes and proposes future directions that can be taken.

# 2. Background

## 2.1 Introduction to Fuel Cells and Metal-Air Batteries

Rising energy demand coupled with rising costs of fossil fuels have spurned interest into the development of sustainable energy technologies. Fuel cells and batteries have been shown to possess the potential to replace the current combustion engine in automotives or to be used as a source of power for portable devices.[3] The main difference between fuel cells and current state of the art batteries is that fuel cells are electrochemical energy conversion devices, whereas batteries are electrochemical energy storage devices. Both technologies are promising in delivering clean and sustainable energy. Fuel cells of all types can be found in a variety of applications, ranging from electric vehicles to power stations. In the case of battery technology, Lithium-ion batteries are currently used in a wide range of applications as well, such as electric vehicles and mobile devices; however, the current state of the technology has reached a plateau in providing sufficient energy density for high energy demand applications such as electric vehicles, limited by the intercalation materials available.[5,6] One approach to increase the energy density of current lithium-ion batteries is to replace the cathode with an air-breathing electrode. These new type of batteries under development are known as metal-air batteries and are similar to fuel cells as they involve the reduction of oxygen gas during discharge.

Fuel cells directly convert chemical energy from a fuel into electrical energy, and thus are far more efficient than combustion engines, reaching approximately 2-3 times higher efficiencies when operating at optimal conditions.[32] A fuel cell consists of two electrodes (an anode and a cathode), separated by an electrolyte. Electrochemical oxidation of a fuel occurs at the anode, producing electrons, and electrochemical reduction occurs at the cathode of the fuel cell. The

electrons produced at the anode travels through an external circuit, powering a load, before entering the cathode.

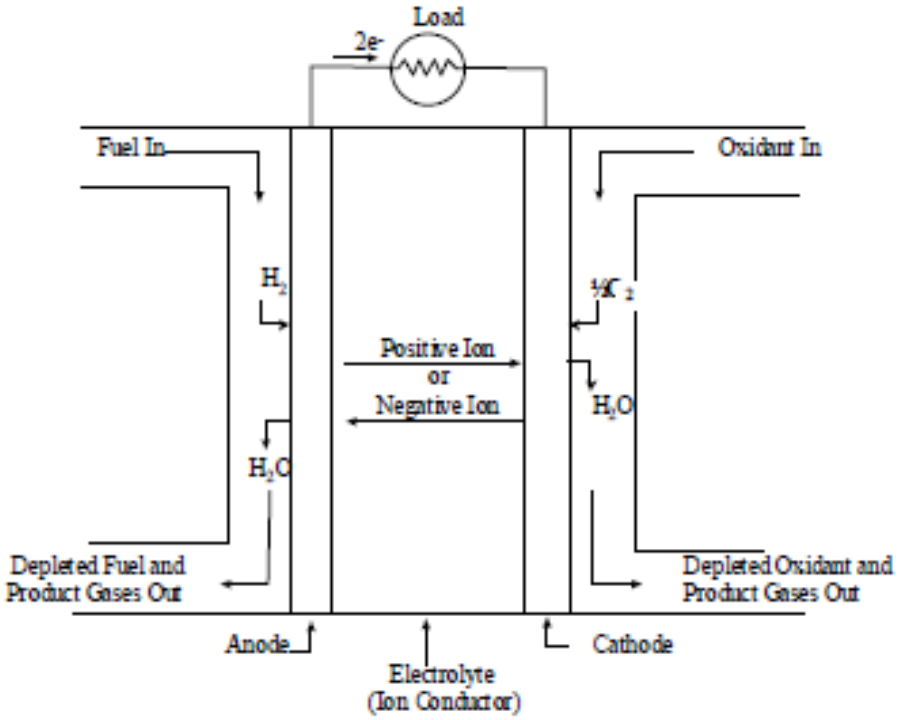


**Figure 2.1.** Schematic showing basic structure of a fuel cell as well as the flow of electrons from anode to cathode.[33]

Once the electrons from the anode enter the cathode, the electrons participate in an electrochemical reduction reaction. In general, hydrogen is often used as the fuel and is oxidized at the anode, and oxygen is reduced at the cathode. The two reactions when combined, results in a general equation where hydrogen and oxygen combine to form water.

$$\text{Anode: } H_2 \rightarrow 2H^+ + 2e^-$$

$$\text{Cathode: } O_2 + 4e^- + 4H^+ \rightarrow 2H_2O$$

$$\text{Full: } \quad 2H_2 + O_2 \rightarrow 2H_2O$$

Due to the fact that the byproduct of fuel cells is simply water, fuel cells are an extremely attractive technology in producing clean energy. Furthermore, both hydrogen and oxygen are abundant materials and as long as fuel is supplied, the fuel cell would be able to supply energy. Each fuel cell can be stacked together forming a fuel cell stack.

Fuel cells can be separated by the type of electrolytes employed, and thus classified as: (i) Phosphoric Acid Fuel Cells (PAFC), (ii) Molten Carbonate Fuel Cells (MCFC), (iii) Solid Oxide Fuel Cells (SOFC), (iv) Alkali Fuel Cells (AFC), and (v) Polymer Electrolyte Membrane or Proton Exchange Membrane fuel cells (PEMFC). Table 2.1-1 summarizes the different categories of fuel cells and their operating conditions.

**Table 2.1-1. Summary of the five different classifications of fuel cells and their operating parameters**

| Fuel Cell Type | Operating Temperature | Electrolyte | Mobile Ion | Start-up time |
|---|---|---|---|---|
| **Phosphoric Acid Fuel Cells** | Low, 150-200 °C | Phosphoric Acid | $H^+$ | Moderate |
| **Molten Carbonate Fuel Cells** | High, 650 °C | Sodium or Magnesium carbonates | $CO_3^{2-}$ | Slow |
| **Solid Oxide Fuel Cells** | High, 1000 °C | Hard ceramic compounds | $O_2^-$ | Slow |
| **Alkali Fuel Cells** | Low, 150-200 °C | Potassium Hydroxide | $OH^-$ | Fast |
| **PEM Fuel cells** | Low, 80 °C | Acidic polymer electrolyte membrane | $H^+$ | Fast |

The different classifications of fuel cells can be further divided based on their operating temperatures, where SOFCs and MAFCs are considered as high temperature fuel cells. These fuel cells require extremely high temperatures to operate efficiently. Especially in the case of SOFCs, the high temperatures are required for the diffusion of oxygen through the solid, ceramic electrolyte. The high temperature required by both fuel cells greatly limits the potential applications of the fuel cells. Furthermore, the need to reach the high temperature first, greatly slows the start-up time of both fuel cells.[34] In this case, for rapid operation, low temperature fuel cells such as AFCs, PAFCs, and PEMFCs, are far more attractive.

Of the low temperature fuel cells, Alkali fuel cells are most often used when high performance is required, and when cost is not a factor. Alkali fuel cells are commonly found in space and military applications. However, the electrolyte of alkali fuel cells is extremely sensitive to water, which means that pure oxygen is required to be fed to the cathode. This greatly increases the operating cost of the fuel cell. Phosphoric acid fuel cells use phosphoric acid as their electrolyte is one of the first fuel cells to have been commercialized. Phosphoric acid fuel cells have the added benefit of having a flexible choice of fuel due to their capabilities of tolerating higher concentrations of carbon monoxide. However, the electrolyte employed is highly corrosive and thus corrosion tolerant materials must be employed. The last category, PEM fuel cells, is also referred to as solid polymer fuel cells as it employs the use of a solid polymer as its electrolyte. PEM fuel cells are a highly attractive type of fuel cell and are often favoured more over other fuel cells. This favouritism for PEM fuel cells is due to the high energy density, low operating temperature, quick start-up time, and rapid response to varying loads exhibited by PEM fuel cells.[3,34] These properties make PEM fuel cells an extremely

attractive option to be used in all manner of applications, including the powering of electric vehicles.

Metal-air batteries are an energy storage device as opposed to fuel cells, where energy is converted form fuel. A metal-air battery consists of a solid metal anode, an air-breathing cathode, and an electrolyte between the two electrodes. The choice of the electrolyte depends on the type of metal-air battery.[5,6] Likewise to fuel cells, metal-air batteries can be classified by the electrolyte used in the cell. Two types of cell systems exist for metal-air batteries where one cell system is moisture sensitive and the other cell system is not moisture sensitive. The cell system that is not moisture sensitive employs an aqueous electrolyte. The cell system that is moisture sensitive employs the use of an organic, aprotic electrolyte.

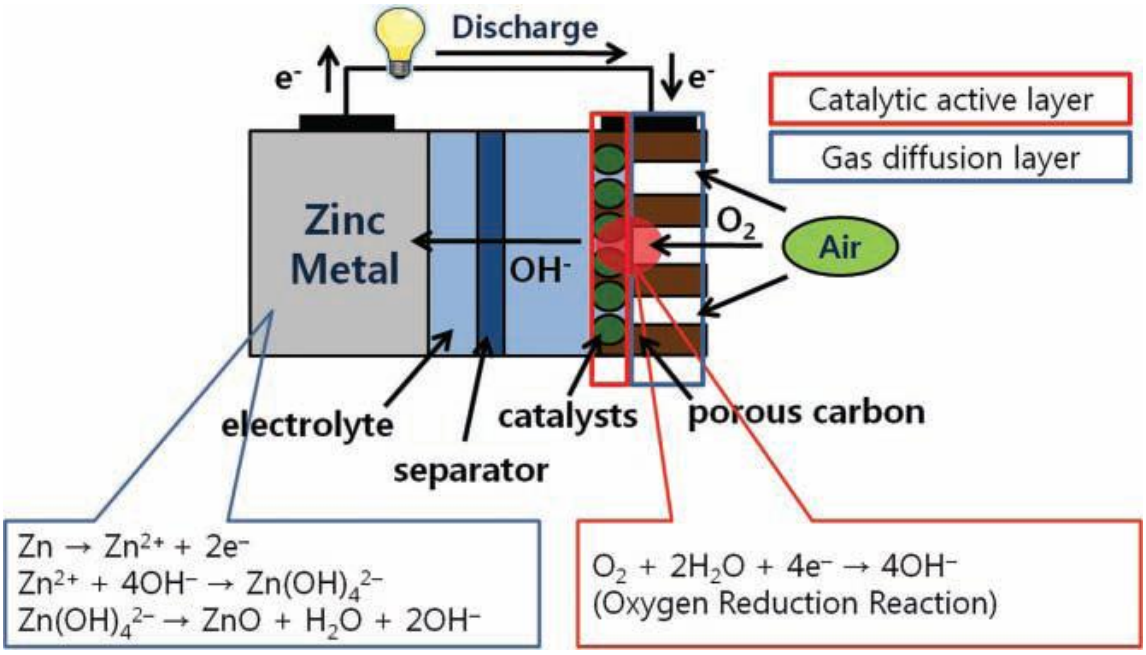


**Figure 2.2.** Schematic of metal-air battery, in this case Zn-air, showing the battery working during discharge.[6]

Aqueous cell systems can employ different types of solid metals as their anode, including, but not limited to: Ca, Al, Fe, Cd, and Zn. Zn-air batteries in particular are exceptionally attractive due to their resistance to corrosion in alkaline solutions, low cost, high shelf-life and a high theoretical energy density of 1084 Wh $kg^{-1}$.[6] For all aqueous cell systems, the operating principle of the battery remains the same.

Metal-air batteries operate in two different modes: charge and discharge. When the battery is in discharge, electrons are released due to the oxidation of the metal anode, producing metal ions. The electrons travel through an external circuit to the cathode where oxygen is reduced forming hydroxyl ions. These hydroxyl ions travel through the electrolyte, past a separator, to the anode where they react with the metal ions to form metal oxides. During charge, the process is reversed and oxygen is evolved at the cathode and the metal oxides at the anode returns to solid metal. Charging of the battery restores the electrochemical materials of the battery to be discharged at later time.[5,6]

## 2.2 Structure of PEM Fuel Cell

In its simplest form, a PEM fuel cell consists of a two bipolar plates and a membrane-electrode assembly (MEA). The MEA is the key component of the PEM fuel cell, combining the electrodes together with the solid polymer membrane sandwiched in between. The MEA consists of the anode, cathode, two gas diffusion layers, two catalyst layers, and the solid polymer electrolyte. Each electrode is in contact with a catalyst layer which in turn is in contact with a gas diffusion layer. The polymer membrane separates the anode layers from the cathode

layers of the MEA, separating the half reactions while allowing protons to travel from the anode to the cathode. The gas diffusion layer is responsible for providing uniform and direct access of fuel and oxidant to the catalyst layer. The catalyst layer is the layer containing the electrocatalysts responsible for catalyzing the hydrogen oxidation reaction at the anode or the oxygen reduction reaction at the cathode.[3]

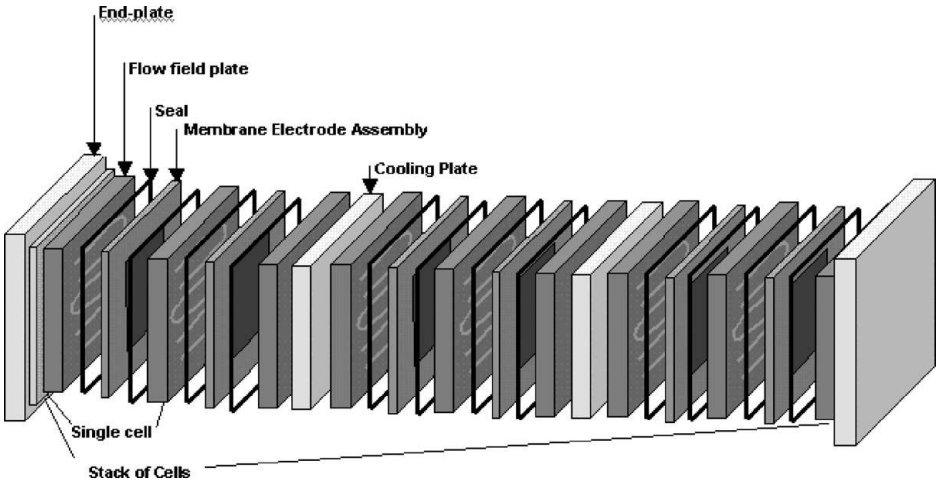


**Figure 2.3.** PEM fuel cell stack.[3]

## 2.3 Structure of Metal-Air Battery

A typical meta-air battery consists of a solid metal anode, an electrolyte, a separator, an air-breathing cathode, and a catalyst. The solid metal anode uses a pure metal as its material. In the case of Zn-air cells, the anode consists of solid Zn. During discharge, oxidation of the metal occurs at the anode. Most of the research does not focus on the anode reaction as the system is relatively simple. As the metal also reacts with the electrolyte, it is possible to improve performance by increasing the surface area of the metal anode particles. The electrolyte lies between the anode and cathode and typically solutions of sodium hydroxide, potassium

hydroxide, and lithium hydroxide are used. Potassium hydroxide is widely used as it exhibits superior ionic conductivity. It is possible that the electrolyte when exposed to air can react with carbon dioxide, forming carbonates and decreasing the concentration of hydroxyl ions. The formation of carbonates and the decrease of hydroxyl ions cause a deterioration of cell capacity. The separator also lies between the metal anode and air cathode within the electrolyte. The main function of the separator is to transport hydroxyl ions ($OH^-$) from the air cathode side to the metal anode side. It is required that the separator be high in ionic conductivity, have sufficient porosity, and be stable in alkaline solution. Typical materials for separators include polyethylene, polyvinyl alcohol, polyolefin, and polypropylene. However, the porosity within the separator may allow metal ions from the anode to travel to the cathode, resulting in a reduction in capacity. Lastly, the air-breathing cathode contains the ORR catalyst and is required to have a highly porous structure to allow inflow of oxygen from air. The cathode is also required to act as a substrate where ORR occurs. Typically the cathode is comprised of a gas diffusion layer and a catalyst layer. The gas diffusion layer is responsible for uniform distribution of oxygen and is often composed of a carbon material and a hydrophobic binder. The hydrophobicity of the gas diffusion layer is important as the layer is required to be permeable to air, but not water. The catalyst layer is the layer that contains the catalyst and is where ORR takes place. These two layers are laminated together to form the cathode.[6]

## 2.4 Fuel cell, Metal-Air Batteries and the Oxygen Reduction Reaction

The oxygen reduction reaction (ORR) occurring at the cathode is the electrochemical phenomena that is shared between metal-air batteries and fuel cells. The performance and efficacy of both technologies significantly depend on the reaction kinetics of the ORR. Often

times, the ORR is the limiting factor in determining the capabilities of the devices, thus the use of ORR active catalysts as part of the electrode materials for both fuel cells and metal-air batteries is commonplace.

## 2.5 ORR in PEM Fuel Cells

The structure of a typical PEM fuel cell and the movement of ions is shown in the figure below. The device consists of an anode, a cathode, and a polymer electrolyte separating the two electrodes. Hydrogen oxidation occurs at the anode, where as oxygen reduction reaction occurs at the cathode.[3,4]

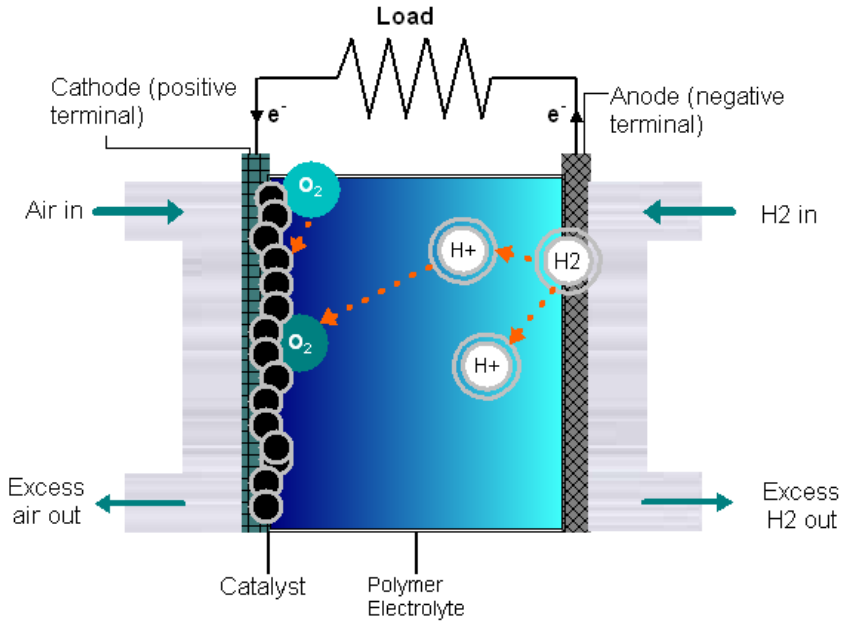


**Figure 2.4.** Schematic showing structure of a typical PEM fuel cell and the oxygen reduction reaction occurring at the cathode.

ORR in PEM fuel cells is the primary electrochemical reaction of concern, occurring at the cathode. ORR in the acidic conditions of a PEM fuel cell can either take a four electron

reduction pathway, occurring at a thermodynamic electrode potential of 1.229 V at standard conditions.

Four electron pathway: $O_2 + 4H^+ + 4e^- \rightarrow H_2O$, 1.229 V

The reaction products differ depending on the pathway taken, where the more efficient and desirable four electron reduction pathway results in the formation of water, whereas the less efficient and less desirable two electron reduction pathway results in the formation of undesirable peroxide species, which, if left unreduced, is capable of causing significant damage to the fuel cell membrane.[1,4,22,29] Additionally, ORR normally suffers from sluggish kinetics, resulting in significant impracticalities in the operation of the fuel cell. Due to the extremely slow nature of ORR and the desire for a four electron reduction pathway, it is imperative to employ the use of ORR active electrocatalysts to assist the reaction to perform at a practical and usable level.

## 2.6 ORR in Metal-air Batteries

A metal-air battery consists of a solid metal anode and an air-breathing cathode that allows oxygen to diffuse to the surface of the electrolyte-cathode interface.

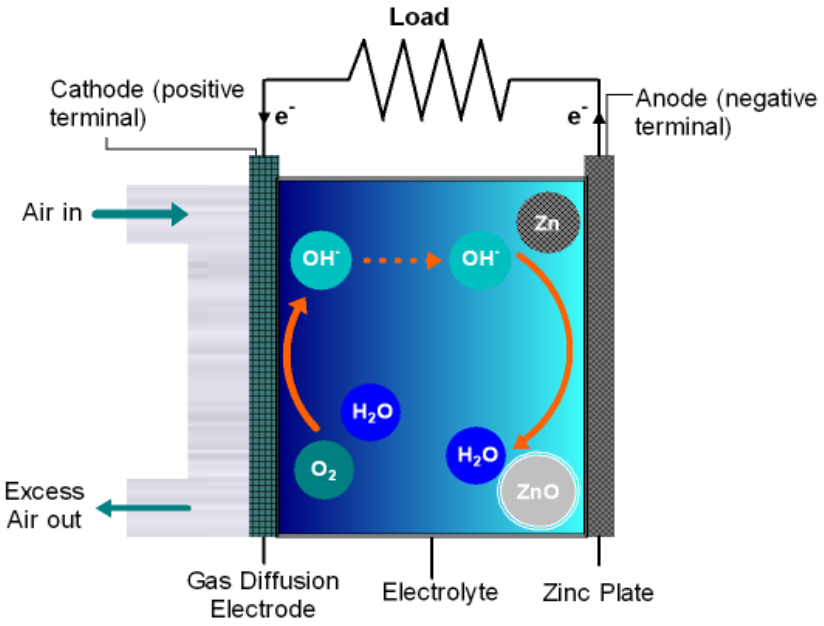


**Figure 2.5.** Schematic showing structure of a typical Metal-air battery and the oxygen reduction reaction occurring at the cathode.

In metal-air batteries, the discharge mechanism of the battery involves the reduction of oxygen into hydroxyl ions, which then travel to the anode of the battery to oxidize the aqueous metal ions. ORR occurs in alkaline conditions also capable of taking either a four electron reduction pathway or a two electron reduction pathway. Again, it is favorable for ORR to undergo the more efficient four electron pathway reduction. ORR occurs at a thermodynamic potential of 0.401 V for a four electron pathway and -0.065 V for a two electron pathway reduction.[4,29]

Four electron pathway: $O_2 + H_2O + 4e^- \rightarrow 4OH^-$, 0.401 V

Two electron pathway: $O_2 + H_2O + 2e^- \rightarrow HO_2^- + OH^-$, -0.065 V

Additionally, in the case of moisture sensitive cell systems employing the use of aprotic electrolytes, such as Li-$O_2$ cells, the oxygen reduction reaction greatly differs, and reduces to a superoxide ion.[4]

## 2.7 Platinum and Non-precious ORR catalysts

Currently noble metal based catalysts such as platinum based catalysts are the only commercially available option in catalyzing ORR. Platinum based catalysts are highly active and stable in both aqueous acidic and alkaline conditions, thus these catalysts are an extremely attractive option to be used in both technological applications. The issue with using platinum catalysts is the high cost associated with the precious metal, which will significantly increase the cost of the device it is used in, introducing further barricades in the commercialization of both PEM fuel cells and metal-air batteries. Although many efforts have been made to reduce the necessary amount of platinum, it does not eliminate the issue that the Earth has a highly limited and low supply of platinum metal. An alternative to the use of platinum based catalysts is to employ non-precious metal catalysts (NPMCs) for the reduction of oxygen.

A number of NPMCs have been investigated to date, beginning with the work of Jasinksi in 1965 regarding the ORR catalytic activity of cobalt phthalocyanine.[26] Jasinski evaluated cobalt phthalocyanine as a potential cathode catalyst in KOH electrolyte and found promising results. Often times this type of transition metal macrocycle catalysts[28,35-41] were supported onto high surface area carbon black, which was found to significantly increase the stability of the catalysts. Cobalt based macrocycles such as Co phthalocyanine or Co porphyrin was found to reduce oxygen through a 2-electron pathway, producing $H_2O_2$, whereas Fe based macrocycles,

such as Fe phthalocyanine, was found to reduce oxygen through a 4-electron pathway, producing $H_2O$.[1,2,36,42,43] Although providing a new avenue of research and showing great promise, the transition metal macrocycles, such as phthalocyanines and porphryins, were exhibiting extremely low stability and were not capable of maintaining their catalytic activity after multiple cycles in acidic conditions.[27,44]

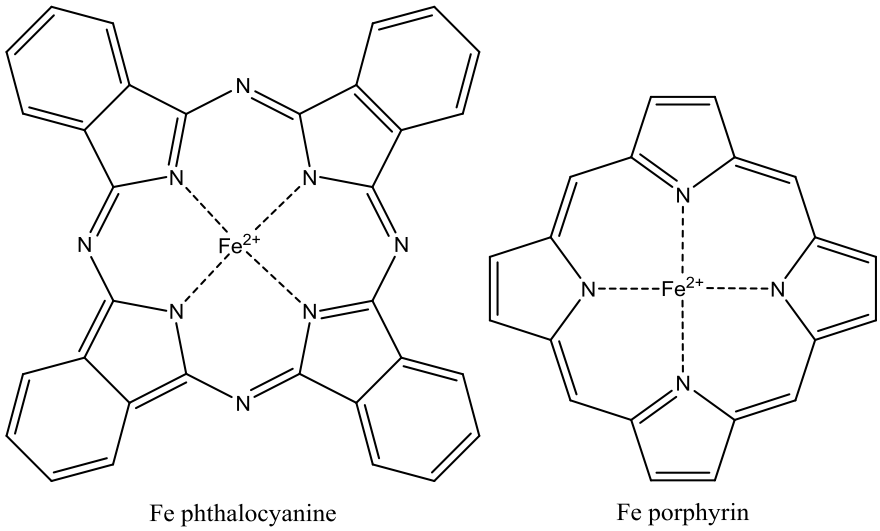


**Figure 2.6.** Structure of Fe phthalocyanine and Fe porphyrin macrocycles. These transition metal macrocycles are commonly used as non-precious ORR catalysts.

Later on, significant improvement regarding the stability and activity of these types of non-precious catalysts were achieved after high temperature pyrolysis of the carbon supported macrocycles.[1,2,4,8,12,45-49] Characterization of the resulting heat treated catalysts indicate that the macrocycle undergoes partial, if not, full decomposition of its structure. This lead to significant questions regarding the active site of heat treated questions, where certain characteristic surface configurations were found after high temperature treatment of the carbon supported macrocycles.[50,51] By employing various spectroscopic techniques, including X-ray,[20,52-54] Mossbauer[52,53,55,56] and mass spectroscopy,[50,51,57,58] M-$N_x/C_y$ and N-C (M is a transition metal)

surface configurations were found and believed to represent the active sites formed after high temperature pyrolysis.[50,51] From this knowledge, a significant breakthrough was made regarding synthesis of heat treated ORR catalysts where it was proposed and shown that the M-$N_4$ chelating structure of a macrocycle is not needed in forming active heat treated catalysts. Instead, it is possible to synthesize active and stable ORR catalysts by heat treating separate nitrogen, carbon, and transition metal precursors. A typical procedure involves filling the pores of a high surface area carbon material with a nitrogen and transition metal precursor followed by heat treatment in an inert atmosphere at temperatures above 600 °C.[1,2,11,18,59] Depending on the structure of the precursors, and the heating temperature, it was possible to obtain different types of surface configurations, such as M-$N_2$/C or M-$N_4$/C,[50,51] which has been proposed to represent different types of active sites. As of now, the identity of the active site of heat treated non-precious catalysts is still in debate.

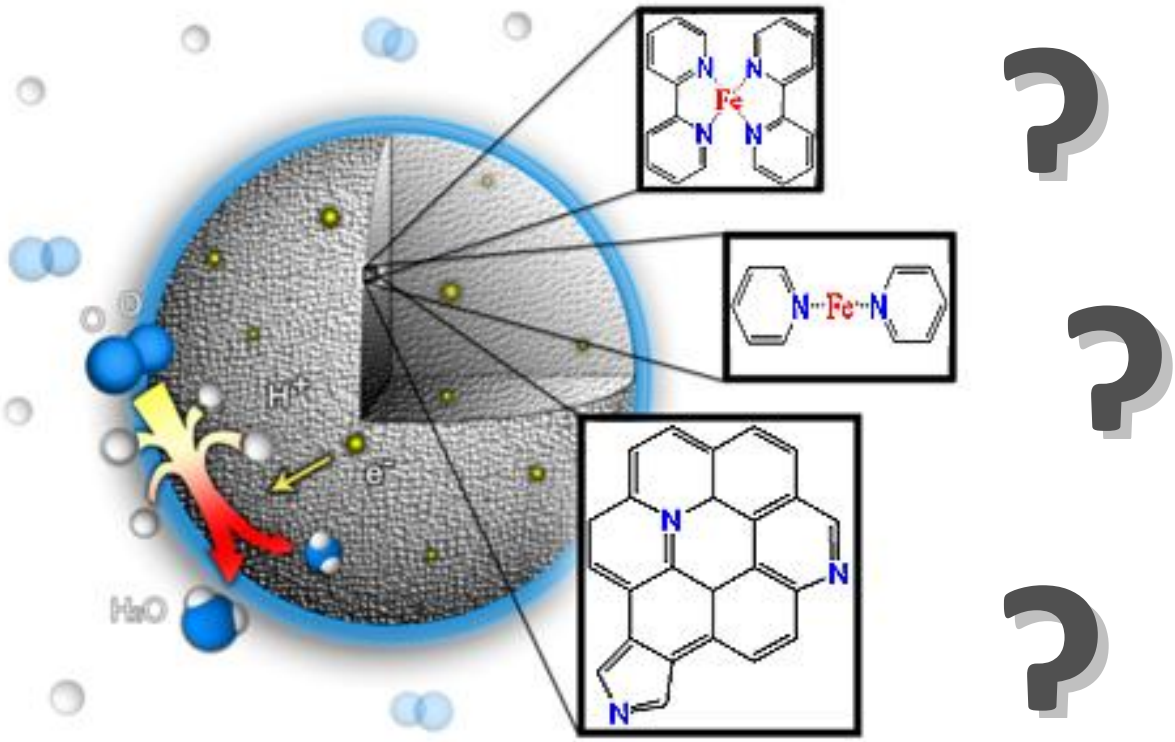


**Figure 2.7.** Types of proposed active sites located in the structure of a carbon support.

The uncertainty of the active sites in heat treated non-precious ORR catalysts often results in a number of trial and error type of experiments in attempting to produce highly active and stable catalysts.[27] The effects of varying the nitrogen precursor or transition metal are commonly studied. A number of different nitrogen precursors have been studied thus far, including phthalocyanines,[21,49,60] porphyrins,[48,61,62] ethylenediamine,[15,20] polyaniline,[11,63,64] cyanamide,[16,65] phenathroline,[18,66,67] ammonia,[65,66] and acetonitrile.[54,68,69] As for the transition metal, the most promising results were obtained by using Fe and Co transition metal precursors. Alternatively, the non-heat treated catalysts, such as Fe phthalocyanine or Co porphyrins, have well defined structures and active sites, thus it is often more rewarding to study ORR mechanics on non-precious catalysts using transition metal macrocycles. However, for practicality and usability purposes, heat treated catalysts show far better results in terms of both stability and

activity. Indeed, recent significant progress was made when non-precious catalysts that were comparable to platinum based catalysts in acidic conditions were synthesized using high surface area carbon with Fe, and FeCo/polyaniline.[11]

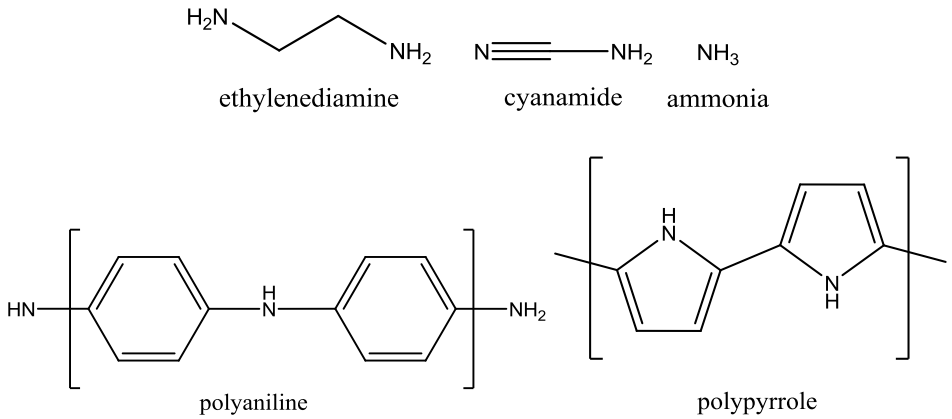


**Figure 2.8.** Chemical structures of commonly used nitrogen containing compounds for synthesis of heat treated ORR catalysts.

. Recent advances in heat treated, pyrolyzed carbon catalysts also focus on the physical structure of the catalysts. Indeed, also in accordance to our own findings, highly active catalysts can be further improved by improving the diffusion and mass transport of reactants to and from active sites. These catalysts are synthesized via introducing sacrificial silica particles into the pyrolysis mixture. After pyrolysis, the silica particles are removed, leaving a numerous pores. The type of sacrificial silica used includes both complex ordered meso-porous structured silica such as SBA-15[70-73] and amorphous silica.[74-77] Typically, highly porous carbon catalysts of this type are synthesized by dissolving a nitrogen containing carbon polymer or organic molecule and adding silica into the solution. After sonication or well mixing, the solvent is evaporated or removed and the resulting substance is pyrolyzed in an inert atmosphere. Once pyrolyzed, the

silica particles or silica template is removed, resulting in porous carbon catalysts. Catalysts synthesized this way exhibited well limiting polarization curves and high limiting currents.

An additional treatment method that is commonly used in literature and in practice is to expose the pyrolyzed catalysts to ammonia either pre- or post-pyrolysis. A large number of research groups report the use of this technique.[11,18,31,78-82] This technique is shown to greatly improve the catalytic activity of carbon based non-precious catalysts. It is speculated that the introduction of ammonia into the system creates micropores and incorporates nitrogen into the structure at the same time.[83,84] The result of which is a highly active and porous catalyst containing high nitrogen content.

## 2.8 ORR mechanism on non-precious catalysts

Heat treated non-precious catalysts exhibit much higher stabilities and activity than transition metal macrocycles, which exhibit catalytic activity towards ORR without high temperature pyrolysis. However, the active sites of catalysts produced by high temperature pyrolysis are not well defined or known. Furthermore, it is very difficult to characterize and identify the structure of the active sites due to the multitude of events that occur during high temperature pyrolysis, and the complexity of the resulting catalyst. In this case, it is beneficial to conduct ORR mechanism studies on non-precious catalysts such as metal phthalocyanines which potentially share similar active site structures ($M-N_4$) and have their active sites well defined. The starting point for oxygen reduction begins with the binding of oxygen gas onto the active site of the catalyst. Studies regarding the adsorption of oxygen onto a surface suggest that the mechanism involves 'backbonding' of the oxygen gas molecule to a binding site.[4,23,24] Backbonding is a concept where the atom that serves as the binding site donates an electron to the π-anti-bonding orbital of an oxygen gas molecule. In this case, the transition metal ion serves as the binding site for molecular oxygen. The process begins with an electron transfer from molecular oxygen to an empty $d_z^2$ orbital of the transition metal ion. The interaction lowers the π*-anti-bonding orbitals of oxygen while raising the $d_{xy}$ and $d_{yz}$ orbitals of the transition metal, allowing the transition metal to donate an electron from its filled orbitals to the unfilled π*-anti-bonding orbitals of oxygen gas. The result is the formation metal/ligand-oxygen adduct.

It has been proposed that the reaction mechanism could proceed as a modified "redox catalysis" process,[4,22] where dioxygen gas first forms an adduct with the metal ion center of the transition metal phthalocyanine as previously described. An intra-adduct electron transfer occurs from the metal to oxygen, and subsequent protonation of the adduct from the electrolyte, results

in the formation of $H_2O_2$. $H_2O_2$ could then be further reduced to water by further electron transfers and addition of protons, or it could remain as the final product. A summary of the mechanism is shown below:

$$[LM^{II}] + O_2 \rightarrow [LM^{\delta+} \ldots\ldots O_2^{\delta-}]$$

$$\left[LM^{\delta+} \ldots\ldots O_2^{\delta-}\right] + H^+ \rightarrow [LM^{III} \ldots\ldots O_2H]^+$$

$$[LM^{III} \ldots\ldots O_2H]^+ + H^+ + 2e^- \rightarrow [LM^{II}] + H_2O_2$$

$$H_2O_2 + 2e^- + 2H^+ \rightarrow 2H_2O$$

In the above mechanism, L represents the ligand and M represents the metal center.

# 3. Experimental Methods and Characterization Techniques

## 3.1 Experimental Methods

### 3.1.1 High Temperature Pyrolysis

A key aspect in producing low cost highly active ORR catalysts is the use of high temperature heating in an inert atmosphere. A typical synthesis procedure begins by loading separate nitrogen and transition metal precursors onto a carbon support. The carbon support is then loaded into a quartz tube to be used in a tube furnace. The tube is saturated with $N_2$ or Ar gas before heated to a typical temperature range of 600 to 1100 °C.

### 3.1.2 Electrospinning

Electrospinning is done by applying an extremely high potential to a polymer solution to eject the material through an air gap onto a grounded electrode which serves as a collector. Electrospinning operates on similar principles as microfiber drawing techniques used in the textile industry. However, in the case of electrospinning, electrostatic repulsion is used as the driving force in drawing fibrers. A typical schematic for an electrospinning setup is shown in Figure 3.1.

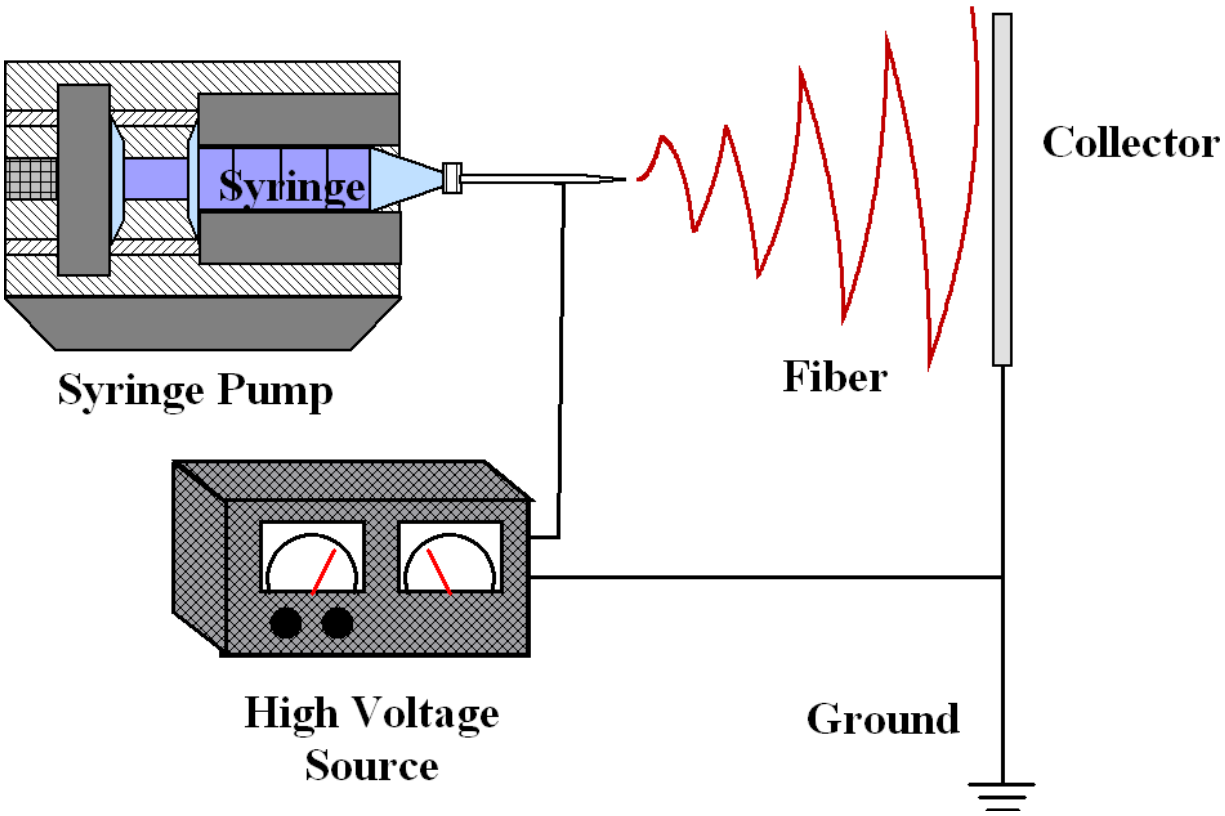


**Figure 3.1.** Schematic showing typical setup for electrospinning.

In a typical electrospinning experiment, a solution containing a conducting solvent or polymer is charged within a syringe while the syringe is pumped at a constant rate with the use of a syringe pump. As a droplet forms on the tip of a needle, it experiences electrostatic repulsion from the build-up of surface charge and the Coloumbic forces due to the applied electric potential. Due to these forces, the droplet will form into a conical shape known as a Taylor Cone. Once the electrostatic forces can overcome the surface tension forces in the solution, a liquid jet will be ejected towards the grounded electrode, undergoing stretching and whipping.[85,86] This results in the formation of fibrous polymers. The electrospinning procedure largely depends on the solution prepared, where thicker or thinner diameter fibers can easily be produced by reducing the concentration of the polymer within the solution.

## 3.2 Characterization Techniques

### 3.2.1 Scanning Electron Microscopy (SEM)

SEM is a technique allowing for high magnification imaging of samples by shooting electrons at a target and detecting the resulting deflected or generated electrons. A sample is prepared on carbon tape and stuck onto a metal stage. The stage is placed inside a vacuum chamber where an electron gun is positioned straight above. The electron gun emits electrons which are than bombarded onto the sample. An image is constructed by detecting the intensity of incoming secondary or backscattered electrons due to the bombardment from the electron gun. The primary instrument used in characterizing the materials discussed and explored in this thesis is the LEO 1550 field emission SEM. An acceleration voltage of 5 kV to 10 kV was applied at a working distance of 10 cm. The surface morphologies and shape of the catalysts were investigated using this configuration.

### 3.2.2 Transmission Electron Microscopy (TEM)

TEM allows for ultra high resolution images at extremely high magnifications, capable of resolving angstrom size features. Instead of detecting secondary electrons in the case of SEM imaging, TEM imaging operates by detecting the intensity of transmitted electrons. The JEOL 2010F was the primary instrument used to investigate the surfaces of the catalysts investigated in this thesis. Catalysts were first dispersed in a methanol before a single drop as dropped onto copper grid to be visualized under a TEM.

### 3.2.3 Brunauer, Emmet, Teller Adsorption Isotherm (BET)

BET adsorption isotherm analysis provides a measure of the surface area or porosity of a material. The surface area of a material is often highly significant in the development of catalysts as a high surface area implies a high density of exposed catalytic active sites. A sample is prepared inside a glass tube and the weight is measured. The sample is baked and vacuumed at roughly 200 °C to remove water that may be adsorbed onto the sample's surface. The sample tube is lowered to liquid nitrogen temperatures and exposed to nitrogen gas where its nitrogen adsorption isotherm is determined. From the obtained isotherm, it is possible to calculate the BET surface area, and determine the porosity of the material. The ASAP 2020 was the primary instrument used.

### 3.2.4 X-Ray Photoelectron Spectroscopy (XPS)

The surface composition of the catalyst is often used to identify the catalytic active sites, which can be determined by the use of XPS. This technique involves the use of x-rays to irradiate a sample, causing the sample to emit electrons due to photoelectric effect. The emitted electrons exhibit specific binding energies associated with where they originate from. The resulting spectrum of intensity of binding energies can be used to determine the elements and the electronic state of the elements present at the surface of the sample.[54,87]

### 3.2.5 X-Ray Diffraction (XRD)

XRD is used in the research to identify the presence of metal particles or metal oxides that may be present after high temperature treatment of the catalysts. XRD is capable of determining the crystal structure of a material by detecting diffracted x-rays and employing Bragg's Law.

$$\sin(\theta) = \frac{n\lambda}{2d}$$

The specific crystal structure obtained from the diffraction results can be used to identify the sample to a specific material. The technique involves sweeping over a range of angles and detecting the intensity of diffracted x-rays. XRD depends on the crystallinity of material and thus does not function when the material is amorphous. The Bruker D8 XRD was used as the primary instrument in investigating the catalysts presented in this thesis.

### 3.2.6 Rotating Ring Disk Electrode (RRDE) and Potentiostat

The rotating ring disk electrode (RRDE) technique is a technique often used in the electrochemical characterization of catalysts along with a potentiostat. A potential range is scanned and the current produced is measured using a potentiostat while the electrode is rotated within an electrolyte filled cell. A catalyst ink is prepared and coated onto an electrode. The electrode consists of a glassy carbon disk, surrounded by a platinum ring. The electrode was designed to be able to provide two current readings; current from the disk and current from the platinum ring. Current from the platinum ring is used as an indication that hydrogen peroxide was formed during the potential sweep. If oxygen is reduced within the center disk electrode

into hydrogen peroxide, the hydrogen peroxide will travel towards the outer platinum ring, and be further reduced, creating current.[4]

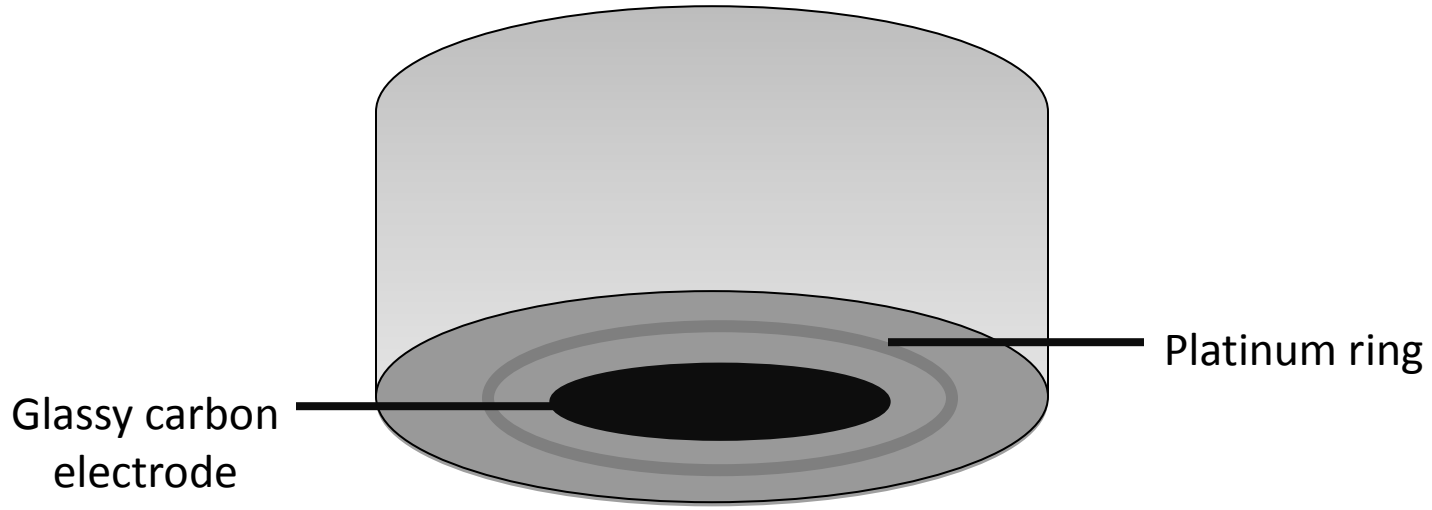


**Figure 3.2.** Rotating ring disk electrode.

### 3.2.7 Half-cell

Half-cell testing only focuses on one half of the electrochemical process and is an easy and quick way to evaluate the efficacy of catalysts. RRDE technique is often employed for half-cell testing conditions. The working electrode is used in conjunction with a reference electrode and a counter electrode in a three electrode setup. These electrodes feed into a electrochemical cell containing an electrolyte. A gas inlet feed is often also connected to feed the desired gas into the system. Changing the rotating speed of the working electrode can change the rate of which reactants are exposed to the catalyst layer.

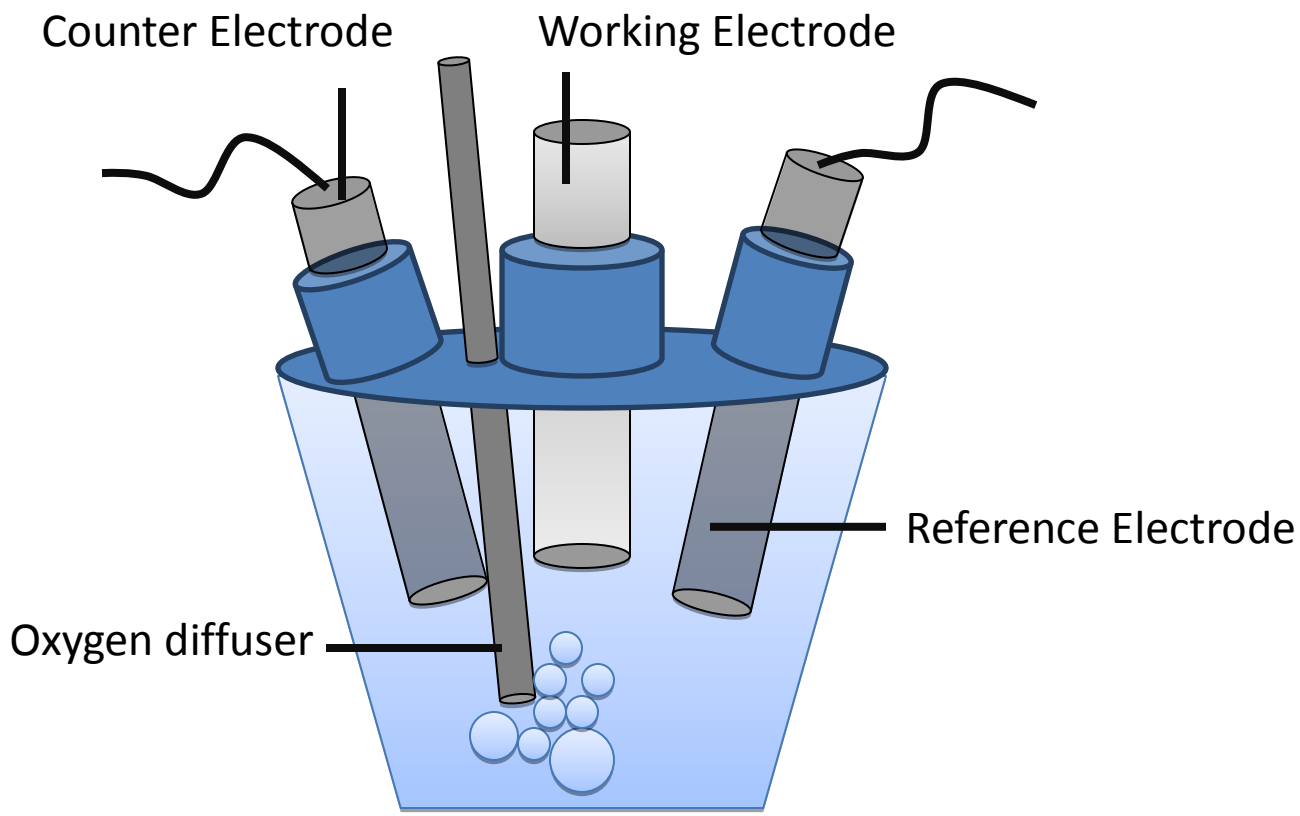


**Figure 3.3.** Electrochemical half-cell setup with a three electrode system and a inlet feed gas.

### 3.2.8 Linear Sweep Voltammetry (LSV)

LSV is an electrochemical characterization technique used to characterize the polarization curve of the catalyst. The potential is linearly swept from one end of a potential range to another and the resulting current is measured and collected. Plotting the current vs. potential curve gives the polarization curve of the catalyst and gives an indication of how active the catalyst is. High limiting currents, positive on-set potentials and positive half-wave potentials indicate active catalysts.

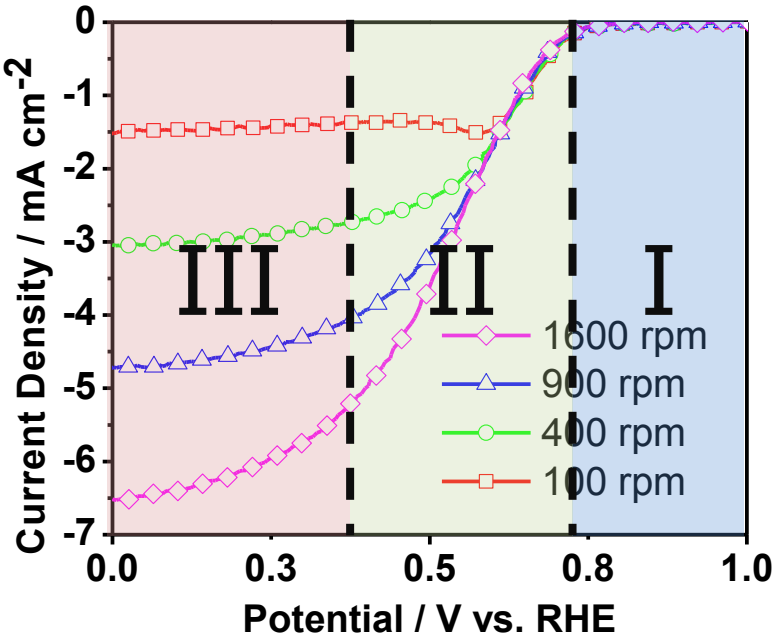


**Figure 3.4.** Typical polarization curve obtained from LSV scan. Regions are marked as I (kinetic region), II (mixed region) and III (diffusion limited region).

Figure 3.4 shows a typical polarization curve obtained after an LSV scan from a positive potential to a negative potential. The main regions are indicated In roman numerals as I, II, and III. These regions correspond to the kinetic, mixed, and diffusion limited regions of a polarization curve, respectively. In region I, the main contributing factor to the curve is the kinetic response of the catalyst. In region II, both kinetic and diffusion factors apply. In region III, the main contributing factor is the diffusion of reactants. In this case, it makes sense that as the rotation speed of the working electrode increases, the current in region III also increases. Furthermore, the half-wave potential of a catalyst (the potential that occurs at half the maximum current) is a good general indication of both the kinetic and mass transport properties of the catalyst. The on-set potential which indicates the potential where the catalyst begins to produce current lies solely in region I and is a benchmark that reveals the kinetics of the catalyst. LSV

employed in nitrogen saturated electrolyte gives the background current associated with the catalyst. The ORR polarization curve is given when LSV is employed when the cell is under oxygen saturated conditions.

### 3.2.9 Cyclic Voltammetry (CV)

Cyclic voltammetry is a common screening technique to identify the capacitance and electrochemical surface species of the catalyst. As the name suggests, the potential is cycled through a range. The potential sweeps from a start voltage to an end voltage, then back to the start, completing the cycle. CV is often employed in nitrogen saturated conditions where no other effects such as ORR occur. Doing so reveals the surface species on the catalyst that are electrochemically active and also reveals the inherent capacitance of the catalyst. Surface species appear as reduction and oxidation peaks on the CV curve. The figure below indicates a typical CV curve.

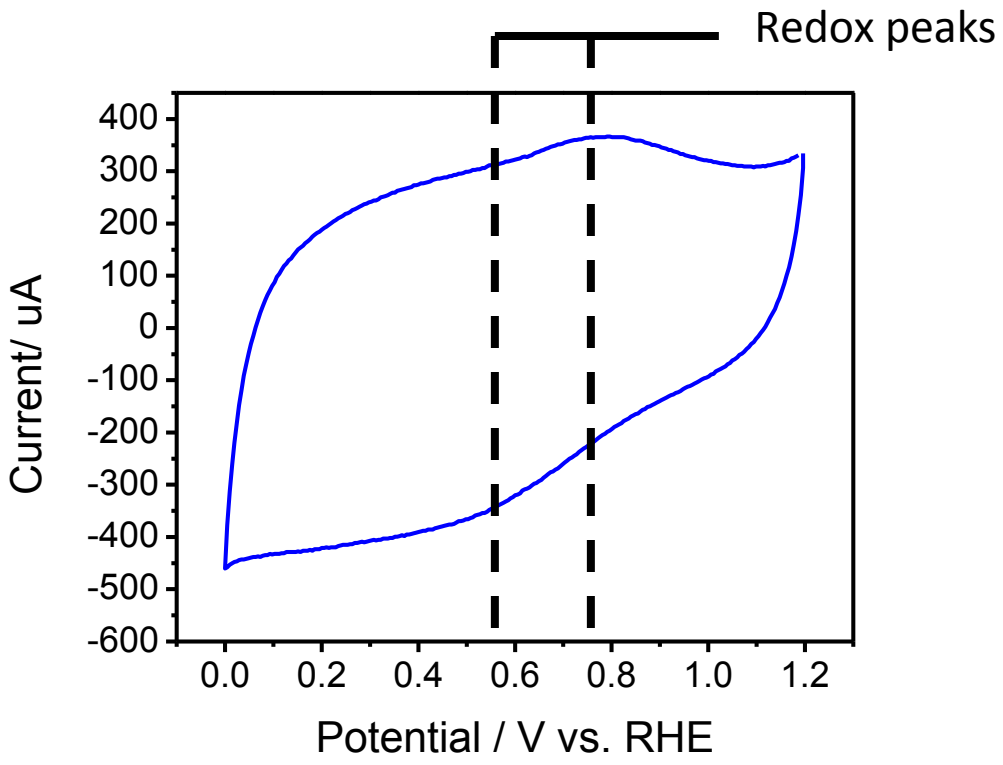


**Figure 3.5.** Typical cyclic voltammetry curve of pyrolyzed non-precious catalysts.

### 3.2.1 Ring current analysis

The ring current obtained from the platinum ring on the rotating ring disk electrode can be used to determine a few key characteristic benchmarks of the catalyst. The $H_2O$ selectivity and the number of electrons transferred can be calculated based on the ring current obtained.[69] The ring current is essentially compared to the overall disk current. A high ratio of disk current to ring current indicates that most of the reaction proceeds along a 4 electron pathway and very little $H_2O_2$ are produced. This indicates that the catalyst is behaving efficiently.

The equations to calculate both the electron transfer number and the $H_2O$ selectivity are shown below.

$$n = \frac{4 * I_D}{I_D + \frac{I_R}{N}}$$

$$\%\ selectivity = \left(\frac{I_D + \frac{I_R}{N}}{I_D + \frac{I_R}{N}}\right) * 100$$

In the above equations, n indicates the number of electrons transferred and % selectivity is the H2O selectivity of the catalyst. $I_D$ corresponds to the disk current and $I_R$ corresponds to the ring measured ring current. N is the efficiency of the electrode to in collecting ring current and it varies between electrodes. This number is given by the manufacturer of the electrode. In our studies, the N of our electrode is 0.24. Ideally, it is best to take current measurements at the maximum peak of the ring current.

# 4. Results and discussion of synthesized non-precious catalysts

Polymer Electrolyte Membrane Fuel Cells (PEMFCs) have garnered plenty of attention in light of increased desirability for clean and sustainable energy due to their high energy efficiency, and operation at relatively low temperatures and pressures. PEMFCs can be used in a variety of applications including both portable electronic devices, providing stationary power, and electric vehicles. In spite of massive developments spanning decades on the PEMFC, the majority of the fuel cell cost remains due to the platinum catalyst employed at the cathode to improve the notoriously slow oxygen reduction reaction (ORR) kinetics. Platinum remains the highest performing and most stable catalyst for ORR in acidic conditions in a PEMFC; however, widespread adoption of PEMFCs demands massive reduction in cost, which can be achieved by providing an alternative to expensive platinum catalysts. Moreover, it is necessary for the long term to replace platinum metal catalysts as the world supply of platinum is limited. The development of non-precious catalysts is encouraged by both demands for lower costs and abundance of available catalytic materials.

Pyrolyzed carbon based non-precious catalysts are alternatives to platinum showing promising results over the past few years. These catalysts are often synthesized via pyrolysis of existing carbon materials. The highest performing carbon based catalysts incorporates nitrogen and are pyrolyzed in presence of a transition metal; however, the activity of these carbon catalysts still fall short of platinum catalysts. A highly active carbon catalyst synthesized from

cheap and abundant materials could be a strong contender in replacing platinum, lowering the cost of PEMFCs, and stimulating commercialization of PEMFCs.

Carbon non-precious catalysts are traditionally synthesized by pyrolyzing carbon black particles in presence of nitrogen and a transition metal. A variety of nitrogen sources have been previously investigated, including small aliphatic molecules such as ethylenediamene, cyanamide, and ammonia, larger nitrogen containing polymers such as polyaniline, polyacrylonitrile, and macrocyclic complexes such as porphyrins and phthalocyanines.

The purpose of this thesis is to advance development and commercialization of PEM fuel cells and metal-air batteries by developing highly active non-precious ORR catalysts. The thesis focuses on the synthesis and investigation of high temperature pyrolyzed non-precious catalysts. This type of non-precious catalyst is synthesized via high temperature pyrolysis of carbon, nitrogen and a transition metal. After pyrolysis, the catalysts were treated with HF acid to remove the silica particles. A number of different

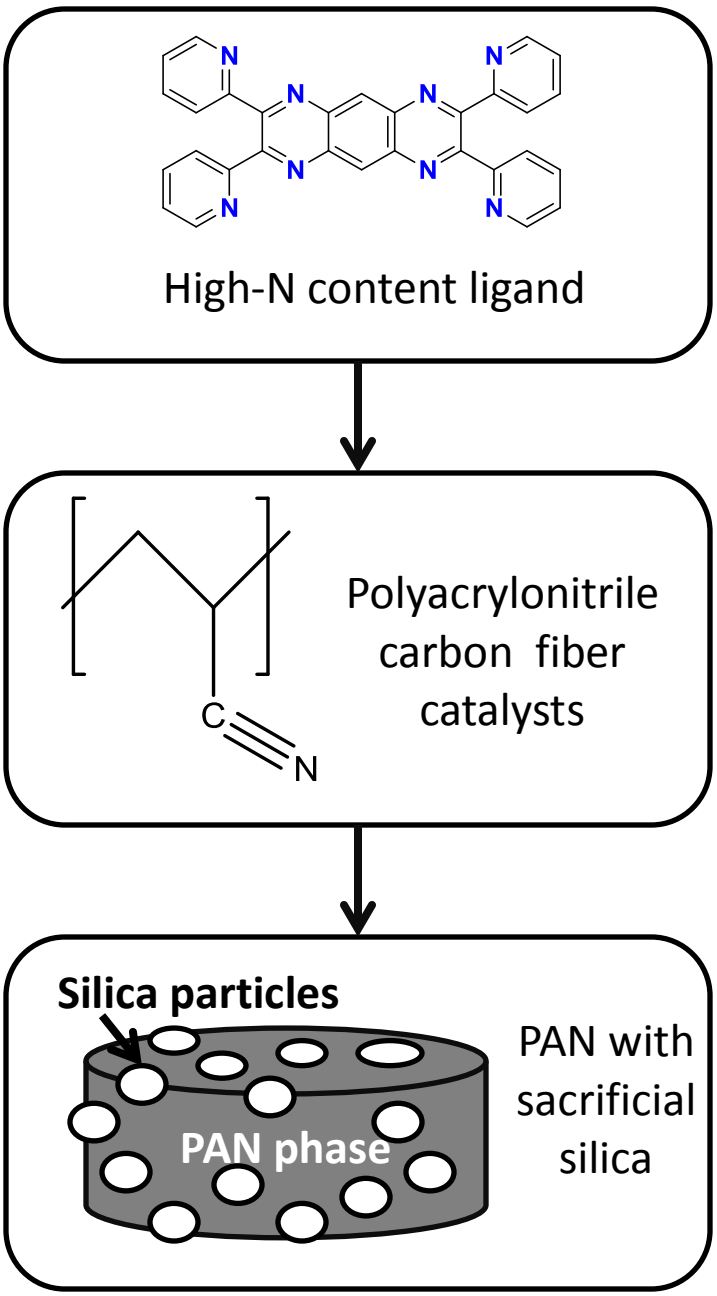


**Figure 4.1.** Scheme summarizing projects investigated during course of research

Three main works has been completed to further the understanding of non-precious catalysts. These three works are further discussed in the section and involve the investigation of heat treated non-precious catalysts. In summary, an initial investigation of a high nitrogen content ligand was done. From the investigation, it was learned that a nitrogen containing ligand

containing high nitrogen content can result in active catalysts, allowing more iron to be used in the formation of active sites. Based on these results, polyacrylonitrile was chosen as the nitrogen containing ligand for further studies. Polyacrylonitrile is a popular material in creating carbon fibers. It is then possible to synthesize carbon fiber electrocatalysts with high nitrogen content by employing the use of polyacrylonitrile. The next two studies investigate electrocatlaysts based on pyrolysis of polyacrlonitrile and an iron salt. The first investigation into the use of polyacrylontrile yielded active catalysts where the activity further improved after acid treatment. Upon investigation, it was shown that acid treatment of the catalyst changes the physical structure of the catalysts, increasing the surface area of the catalysts. The biggest change seen between the catalysts was in the limiting current whereas the on-set potential remains the same between the acid treated and non-acid treated catalyst, indicating that the active sites of the catalysts seem to remain intact. Extending what was learned, the third investigation focuses on improving the catalytic activity of the catalysts by further improving the physical structure of the catalyst that is the porosity and surface area of the catalyst. In this last investigation, the sacrificial silica particles were introduced and removed post pyrolysis. The results in the investigation indicated that significantly higher surface areas and porosity can be achieved by using a sacrificial template to create voids in the carbon structure. Doing so significantly improves the limiting current and half-wave potentials of the polarization curves of the catalyst.

## 4.1 Effects of using a nitrogen-rich ligand in heat-treated non-precious ORR catalyst

### 4.1.1 Introduction

In this study, a nitrogen-rich ligand was designed and synthesized to be used along with an iron metal precursor and a high surface area carbon support in forming active ORR catalysts after high temperature pyrolysis. High temperature treated catalysts are more promising as they provide higher activities and stabilities than their non-heat treated counterparts. The nitrogen-rich ligand, 2,3,7,8-Tetra(pyridin-2-yl)pyrazino[2,3-g]quinoxaline (TPPQ), was designed to mitigate issues that will lower the activity of a catalyst after pyrolysis while possessing a structure that promotes excellent catalytic activity after pyrolysis. Due to the high temperature treatment of the catalyst, sintering of the ionic iron into metallic iron is inevitable. These iron particles were previously discovered to be detrimental to the activity of the catalyst, thus avoiding the formation of iron particles is to be considered. Additionally, nitrogen in the catalyst was found to be a key ingredient along with the transition metal to form highly active catalysts, and thus likely a key component in forming catalytic sites. In order to meet both goals, the nitrogen-rich ligand, TPPQ, was designed to possess a high atomic number of nitrogen, and to discourage the formation of iron particles during the high temperature treatment process. To meet these goals, the nironge-rich ligand possesses a bulky aromatic carbon structure that is stable at high temperatures. The ligand will impede the migration of iron by maintaining their position between the chelated iron ions, discouraging the agglomeration of iron. Furthermore, the ligand possesses extremely bulky aromatic carbon rings that ensure that the ligand-iron complex remains well isolated, allowing for the formation of well dispersed and isolated active

sites. Finally, the ligand possesses a large number of highly stable pyridinic nitrogen that will remain after the high temperature pyrolysis.

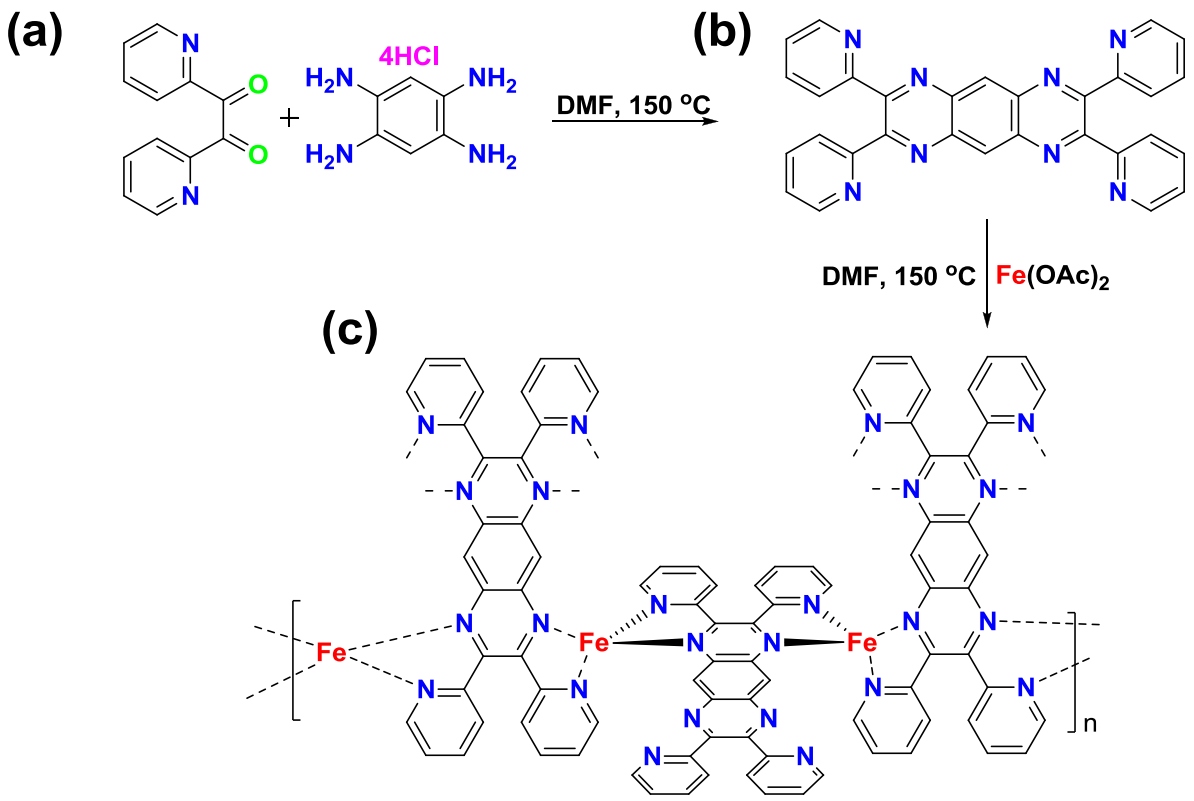


**Figure 4.2.** Structure and schematic of the synthesis of the TPPQ ligand

## 4.1.2 Experimental

The nitrogen-rich ligand, TPPQ, was synthesized by a direct synthesis of the precursors 2,2'-pyridyl and 1,2,4,5-benzenetetraamine tetrahydrochloride. A typical synthesis procedure begins with suspending 0.60g of 2,2'-pyridyl and 0.088g of 1,2,4,5-benzenetetraamine tetrahydrochloride in 3mL of DMF. Both solutions are mixed together and heated a 150 °C and refluxed for a total of 1 hour. The mixture is then allowed to cool to room temperature and the

resulting precipitate is filtered, washed with methanol, and allowed to dry overnight. After synthesis of the ligand, TPPQ is allowed to coordinate with iron by adding the ligand into a solution of iron (II) acetate in DMF. A typical procedure involves dissolving 10mg of the ligand into a 20mL solution of DMF and 3.5mg of iron (II) acetate while stirring. The temperature is raised to 150 °C and stirred to allow the ligand to coordinate with the iron ions. After 1 hour, the mixture is cooled, and 100mg of carbon black (Ketjen Black EC600) is added into the mixture. Once again, the temperature is raised, stirred, and allowed to sit for 1 hour, thereby allowing the coordinated ligand-iron complex to fill the pores and coat the surface of the carbon black support. The resulting ligand-iron/carbon mixture is filtered, washed with distilled water, and dried overnight before entering high temperature pyrolysis in $N_2$ gas saturated conditions at 900 °C for 30 minutes.

After synthesis of the catalyst, 2mg of the catalyst is dispersed in a 1mL solution containing ethanol, Nafion, and water. 20uL of the catalyst ink solution is taken and coated onto a glassy carbon ring disk electrode. The catalyst is then characterized using cyclic voltammetry and linear sweep voltammetry using a rotating ring disk electrode and a potentiostat. Further characterization of the catalyst was conducted using FTIR, Electron Ionization Mass Spectroscopy (EI-MS), SEM and TEM imaging, XRD, and XPS.

### 4.1.3 Results and discussion

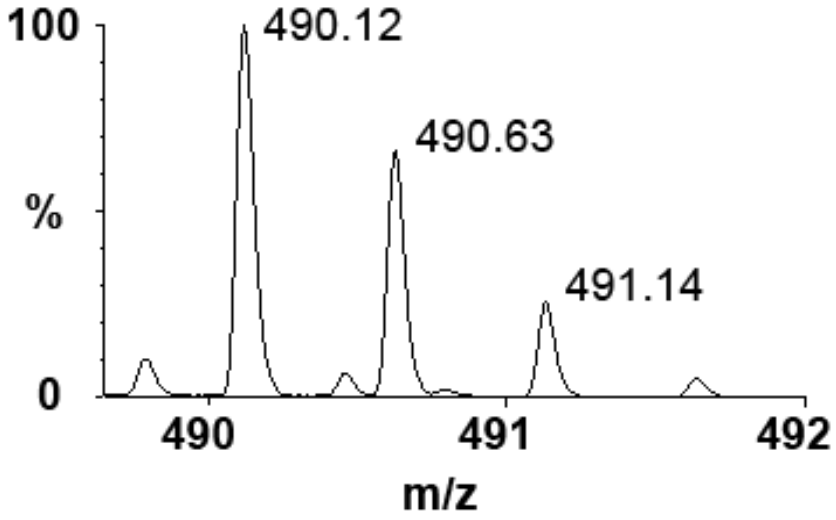


**Figure 4.3.** EI-MS spectrum of TPPQ ligand confirming structure

The structure of the nitrogen-rich ligand, TPPQ, was first confirmed via use of EI-MS. Key peaks were found at 490.12 m/z, 490.63 m/z, and 491.14 m/z with the largest peak centered at 490.12 m/z. These peaks closely correspond to both the theoretical molecular weight of the compound and the predicted mass spectrum. Further characterization of the structure of the ligand by FTIR spectroscopy shows key peaks at 1589 $cm^{-1}$, 1471 $cm^{-1}$ and 1332 $cm^{-1}$ which correspond to the ring stretching vibrations associated with the C=N and C=C ring stretching, and at 779 $cm^{-1}$, 742 $cm^{-1}$, and 711 $cm^{-1}$ which corresponds to the out-of-plane C-H bending (Figure 4.4). Additionally, it can be seen that the characteristic carbonyl doublet peaks at 1717 $cm^{-1}$ and 1695 $cm^{-1}$ of 2,2'-Pyridil disappears in the spectrum of the synthesized ligand, further confirming the formation of TPPQ.[88] These peaks identify the pyridinic nitrogen groups which are the key aspects of the precursor.

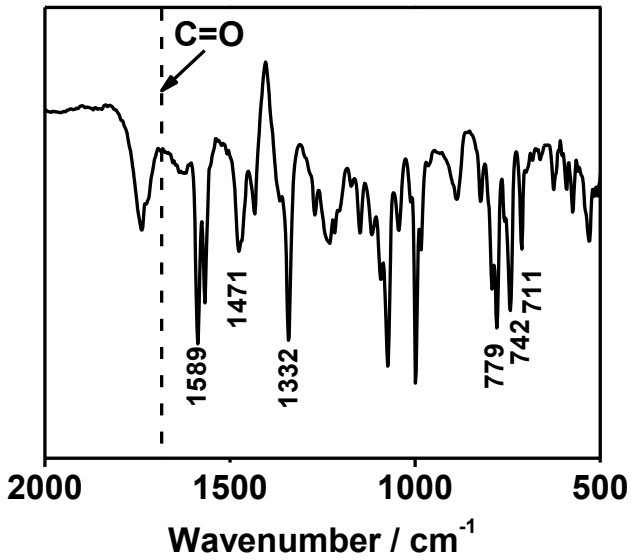


**Figure 4.4.** FTIR spectrum of TPPQ ligand confirming structure

The overall catalytic activity of a catalyst can be increased by either improving upon its intrinsic active site turnover frequency or by increasing the surface density of active sites. Taking the stance that the catalytic site exists in some form on graphitic edge planes as a result of iron and nitrogen,[18,31] it can be logically declared that higher concentrations of iron will result in higher concentrations of active sites. Of course, the consequence of increasing iron content is the saturation of nitrogen sites and the eventual formation of metal or carbidic iron particles. As previously discussed, the design of TPPQ is intended on increasing the density of active sites by allowing for higher iron loadings while discouraging the formation of large iron particles. In this case, a reasonable benchmark in gauging the efficacy of the new catalyst is to determine the existence of large iron particles after heat treatment. To do so, XRD and TEM surface analysis was utilized to confirm the existence of agglomerated iron metal or carbidic iron. The XRD spectrum of catalysts with different initial iron loadings can be seen in Figure 4.5. From Figure

4.5, it is possible to see the emergence of three distinct key peaks signifying iron particle formation at 44°, 45°, and 51° as the iron content increases.[49,89,90]

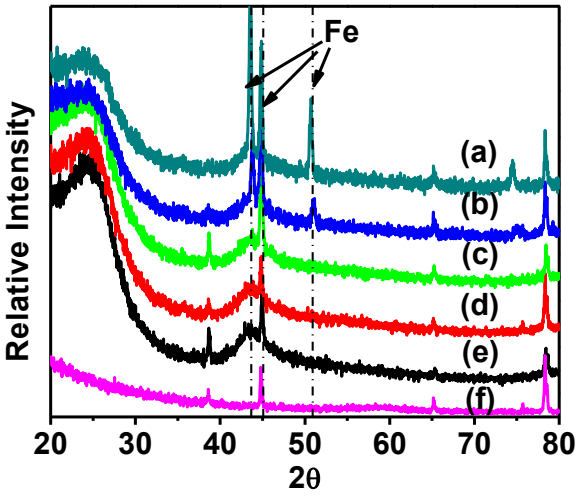


**Figure 4.5.** XRD spectra of catalyst samples with (a) 8%, (b) 4%, (c) 2%, (d) 1%, and (e) 0.5% iron loadings. (f) is the XRD spectrum of the sample holder.

These three peaks indicate the formation of large iron particles, in particular, the formation of α-Fe. A strong, distinct peak was observed in the 4% and 8% iron catalysts, indicating the formation of highly crystalline iron particles. In the case of the 2% iron catalyst, the same strong and defined peaks that indicate iron particle formation were not observed. The lack of iron particle formation in the catalyst with 2% iron loading is further emphasized with TEM images as seen in Figure 4.6. The TEM images of the catalyst shows the expected graphitic structure due to heat treated carbon black, while showing no evidence of iron particle formation of any kind. For the catalysts with higher initial iron loadings, large iron particle formations can be distinctively seen and are shown in the TEM images in Figure 4.7. Based XRD characterization and TEM imaging, it can be seen that our nitrogen-rich ligand is capable of preventing agglomeration of iron up to an initial iron weight percent of 2%, whereas it has

previously been discussed that an iron content of 0.2% is the maximum before iron particles are observed after pyrolysis. However, higher iron loadings still result in large iron particle formation.

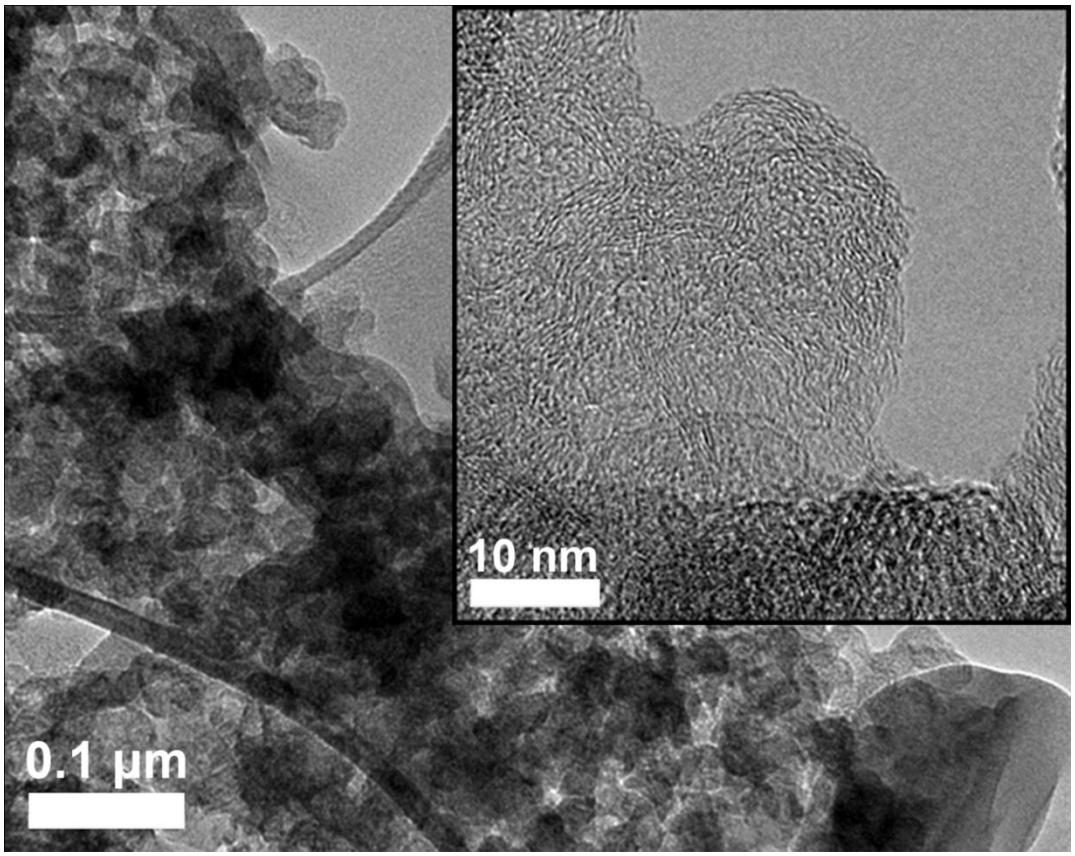


**Figure 4.6.** TEM imaging of Fe-TPPQ catalyst on carbon support after high temperature pyrolysis.

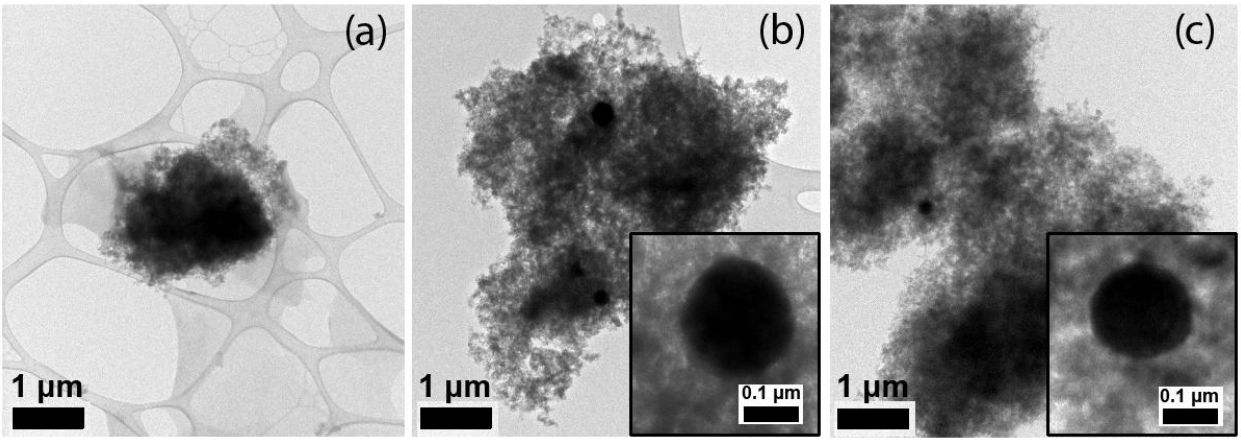


**Figure 4.7.** TEM micrographs for (a) 2%, (b) 4%, and (c) 8% initial iron loading catalysts. Both 4% and 8% catalysts exhibit large iron particle formation.

The Fe $2p_{3/2}$ spectra of all synthesized catalysts were examined and are shown in Figure 4.8. At all initial iron loadings, distinct peak(s) can be found in the Fe $2p_{3/2}$ region, which indicates the presence of iron in all of the examined catalysts. The oxidation states of surface iron can be interpreted from the spectra, where inactive iron carbides or Fe(0)[50,87,91] can be found at 706.7-706.9 eV and 706.7-707.2 eV respectively, Fe(II) at 707.1-708.7 eV, and Fe(III) at 710.8-711.8 eV.[90,91] The median values of the non-ionic and ionic iron species are indicated by the vertical dashed lines in Figure 4.8. A distinct shift towards lower binding energies can be seen in the spectra with increasing initial iron loading.

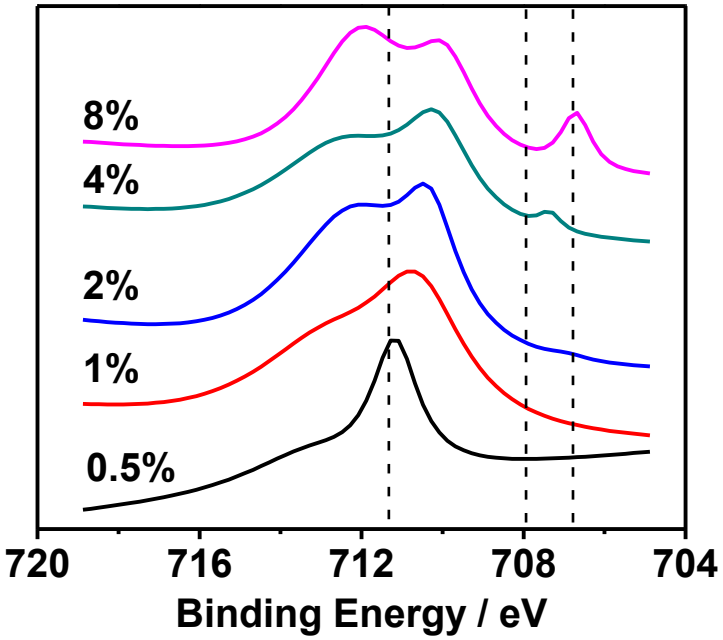


**Figure 4.8.** Fe2p XPS scan of Fe-TPPQ catalyst with different iron loadings.

At initial iron loadings of 4% and 8%, a new feature corresponding to iron carbides and Fe(0) appears, likely indicating the appearance of iron aggregates. The iron aggregate feature in the 4% case is slightly shifted towards higher binding energies as is consistent with the overall trend. The additional iron carbide and Fe(0) feature agrees well with previous XRD and TEM results showing the formation of iron particles at the 4% and 8% initial iron loadings. Additionally, in all catalysts, distinct peaks can be found in the Fe(III) region, indicating the presence of oxidized iron species in the catalysts. The Fe(III) peak dominates in all catalysts, which suggest that the majority of surface iron exists in an ionic state. These surface iron ions could potentially be the metal species bound to nitrogen as indicated in the N 1s scans.

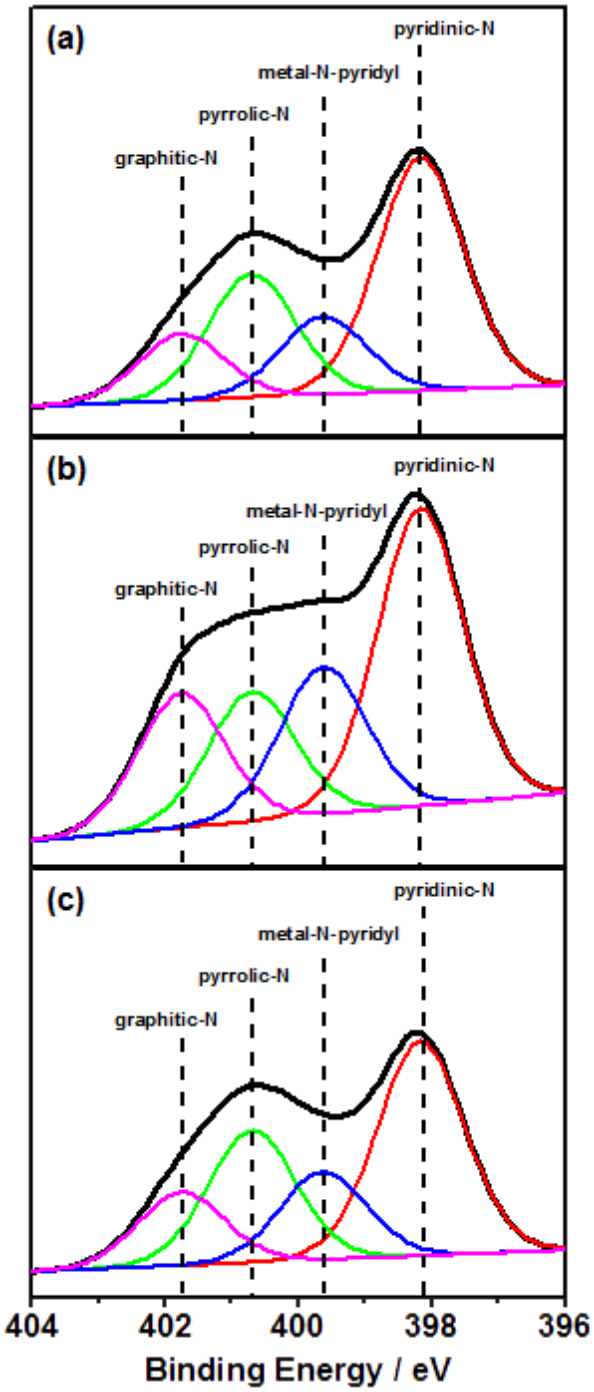


**Figure 4.9.** N 1s XPS scan of Fe-TPPQ catalyst with (a) 1%, (b) 2%, and (c) 4% iron loadings.

The discussion of catalytic activity is often associated with the electronic structure of nitrogen. The electronic structure of nitrogen within the graphitic carbon plays an important role in the activity of the catalyst. To better explain the resulting activities of the catalysts, XPS analysis was performed to identify the relative composition of nitrogen and iron in the graphitic system. The N 1s XPS spectra of three catalysts with different initial iron content, 1%, 2%, and 4%, are shown in Figure 4.9. From the resulting spectra and its fitted peaks, it is possible to identify four peaks related to the different states of nitrogen; pyrdinic nitrogen at 398.2 eV, metal-nitrogen at 399.6 eV, pyrrolic nitrogen at 400.7 eV, and graphitic or oxidized nitrogen at 401.8 eV.[45,46,54] Comparing the three catalysts, it is possible to see that both the 1% and 4% catalysts resulted in a loss of both the metal-bound nitrogen and the pyridinic nitrogen identified by the reduced metal-N-pyridyl and pyridinic peaks. The difference in peak intensities indicates that for 1% and 4% catalysts less nitrogen exist in both the M-$N_x$ state and pyridinic state compared to the 2% catalyst case. The relative higher proportion of M-$N_x$ and pyridinic nitrogen in the 2% iron catalyst suggests that the 2% iron catalyst could contain a higher density of active sites. Additionally, pyridinic nitrogen indicates a higher proportion of exposed graphitic edge planes where the active sites are located.[18,31,54,92] Since pyridinic nitrogen exists on the edge of graphitic planes, a higher proportion of pyridnic nitrogen coupled with evidence of increased M-$N_x$ states signify a higher volume and density of exposed active sites, thus it is not unexpected for the 2% catalyst to be the most active among the three.

The catalytic activities of all five catalysts are evaluated using linear sweep voltammetry in a three electrode cell, using 0.1 M $HClO_4$ as the electrolyte solution. The polarization curves comparing the activities of each catalyst shown in Figure 4.10 is consistent with our XPS results,

with the most active catalyst to be the catalyst with the most iron content while avoiding iron particle formation at 2% initial iron loading.

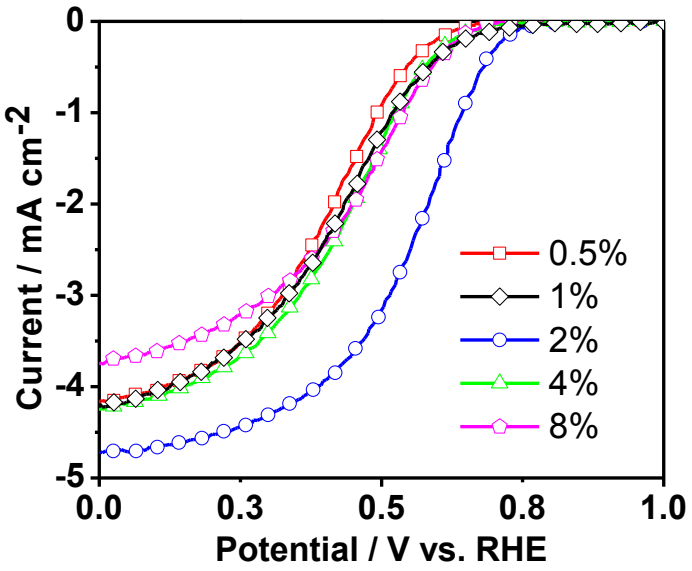


**Figure 4.10.** Comparing the ORR activities of different iron loadings for the Fe-TPPQ catalyst

The 2% iron loading catalyst with the best ORR performance as seen in Figure 4.10 displayed a half-wave potential of 0.52 V vs. RHE with a 4.7 $mAcm^{-2}$ limiting current at a rotation rate of 900 rpm. As stressed a number of times, it is believed that the transition metal along with nitrogen are key aspects in providing catalytic activity, thus it is not irrational to expect higher iron content catalysts to provide a higher surface density of active site structures. Higher iron content suggests that more iron is capable of coordinating with the available nitrogen atoms in the system, especially with the use of a highly nitrogen-rich precursor. At the highest of loadings, the formation and agglomeration of the iron particles negatively affect the catalytic performance, whereas at lower iron loadings, the formation of active sites has yet to be fully saturated.

The cases of lower and higher initial iron content deviating from 2% resulted in relatively lower metal-bound and pyridinic nitrogen. The observed lower concentration of metal-bound and pyridinic nitrogen could be the result of two cases of (a) lower and (b) higher initial iron content: (a) When the initial iron content is lower than optimal, there is insufficient iron present in the system to saturate the available nitrogen sites and hold the coordination of the ligands in place. (b) Once the iron content has exceeded an optimal, saturated value, agglomeration of iron occurs and results in the loss of the coordination between iron and the ligands. The comparison of results obtained for (a) lower and (b) higher iron loadings to that of an optimal initial loading suggest that the use of an optimal initial loading allows for a two-fold benefit of forming more active sites and exposing more graphitic edges after pyrolysis. Assuming the nature of the active site and the intrinsic activity of the active site remains constant with different initial iron content, the consequence of using a non-optimal initial iron loading not only suggests a decrease in active site density as seen from the ORR evaluation and N 1s XPS specta, but can also suggests a decrease in exposed graphitic edge planes as implied by the N 1s XPS spectra. As some form of active site exists at the graphitic edges of the micropores,[18,31,54,92] the decrease in exposed graphitic edge planes is synonymous with the reduction in active site density, and the results agree well.

The associated ring currents and analysis of the ring currents for the 2% initial iron loading catalyst can also be seen in Figure 4.11. From these figures, it is possible to see that the catalysis of oxygen reduction proceeds along a four electron pathway. The number of electrons, n, calculated from the ring currents can be seen in Figure 4.11 along with the $H_2O$ selectivity. Both n and $H_2O$ selectivity were calculated via analysis of the ring and disk currents with the following equations:

$$n = 4 \times \frac{I_D}{I_D + (\frac{I_R}{N})}$$

$$H_2O\ selectivity = \frac{I_D - \left(\frac{I_R}{N}\right)}{I_D + \left(\frac{I_R}{N}\right)} \times 100\%$$

Where $I_D$ is the disk current, $I_R$ is the ring current, and N is a constant used to account for the ring current collection efficiency. The calculated n and $H_2O$ selectivity values approach four and 100% respectively, which provide indication that the catalysis mainly proceeds along a four electron transfer pathway.

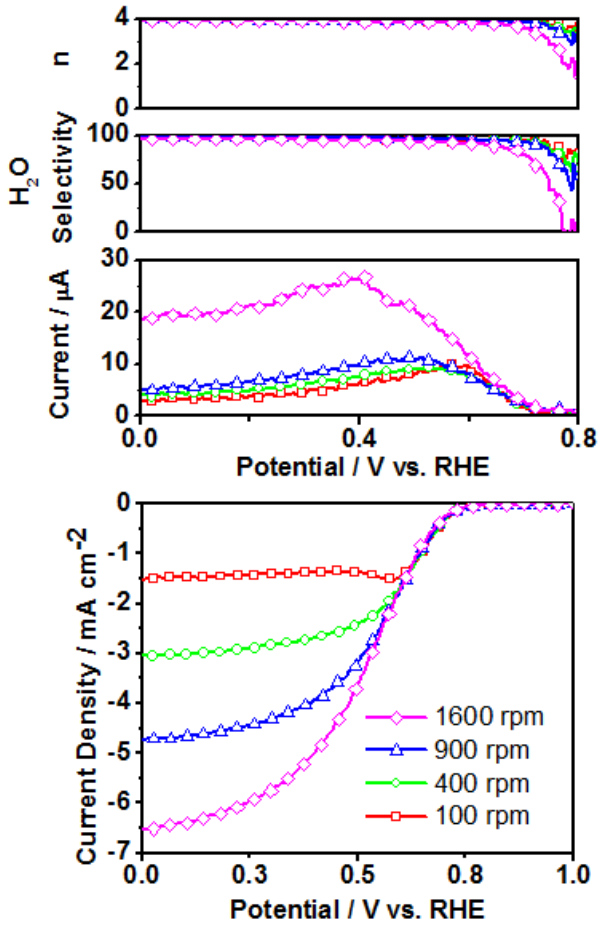


**Figure 4.11.** ORR polarization curve and ring current analysis of Fe-TPPQ catalyst with an optimal iron loading of 2% in $O_2$-saturated 0.1M $HClO_4$.

### 4.1.4 Summary

The results obtained from this work indicated that it is possible to influence the resulting heat treated catalysts by purposefully designing and using specifically structured ligands. Specifically, the issue regarding agglomeration of iron during high temperature pyrolysis was discouraged through the use of a nitrogen-rich ligand with steric hindering groups, allowing for the formation of highly isolated active sites. This result opens up different possibilities in using the nitrogen ligand to influence the final product of the catalyst. In addition, using a nitrogen

rich carbon ligand could greatly increase the ease in producing active pyrolyzed carbon catalysts and allows for more iron salt to be used. In this case, it is imperative that the choice of nitrogen ligand contains high nitrogen content. Additionally, based on the ORR polarization curves, XRD and TEM results, it can be seen that the iron particles still do exist even in the most active catalyst. Further treatment of the catalyst such as acid treatment could improve the activity of the catalyst.

## 4.2 Electrospun Iron-polyacrylonitrile nanofibers as non-precious ORR catalysts

### 4.2.1 Introduction

Electrospinning is an excellent technique that can produce nanofibrous materials with ease. In this study, a web of anisotropic one-dimensional nanofibrous catalysts was synthesized via electrospinning. In the current work, nanofibrous pyrolyzed catalyst using iron and polyacrylonitrile as both a carbon and nitrogen source are synthesized and evaluated for their catalytic activity. A solution containing polyacrylonitrile and iron acetate was electrospun to form the nanofiber morphology. After stabilizing the fibers in air, the fibers undergo high temperature pyrolysis, producing highly conductive carbon nanofibers that are also active towards ORR. These nanofibrous catalysts can also be arranged into a porous electrode structure, allowing for excellent mass transport properties for the reactants of a PEMFC. To improve the activity of the catalyst, the catalyst undergoes a second high temperature pyrolysis treatment after acid leaching, resulting in porous nanofibers. The acid treatment involves immersing the nanofibrous catalysts in 0.5 M $H_2SO_4$ with constant stirring for a total of 24 hours. Although this treatment followed by a second high temperature prolysis results in catalysts with higher activity, it is difficult to predict the outcome the treatment will have on the durability of the catalysts. The resulting catalyst obtained after high temperature treatment was investigated for its ORR activity and characterized via XPS, BET, SEM, and TEM analysis.

### 4.2.2 Experimental

A solution of 5 wt % PAN in DMF along with 0.2 wt % of iron from iron acetate was electrospun at a distance of 13 cm between the tip of the needle and a grounded collector with an applied potential of 13 kV. The nanofibers are collected, dried, and pre-oxidized at 250 °C for 3 hours in air before being carbonized at 900 °C for 30 minutes in Ar gas. The resulting catalyst was named as FePAN-PL (where PL stands for pre-leached).

FePAN-PL is taken and treated with 0.5M sulfuric acid at 80 °C for 24 hours to remove surface iron particles. The FePAN nanofibrous catalyst is filtrated, thoroughly washed, and dried overnight before entering a second pyrolysis at 900 °C in Ar for 30 minutes.

Electrochemical characterization of the FePAN nanofibrous catalyst was carried out via RDE technique, first by preparing a catalyst ink with a concentration of 2 mg/mL. The ink was then deposited onto a glassy carbon electrode 8 uL at a time for five times before applying 8 uL of 0.5 wt % Nafion solution. Linear sweep curves were obtained for the FePAN nanofibrous catalyst at 100 RPM, 400 RPM, 900 RPM, and 1600 RPM in $O_2$ saturated 0.1M KOH, and 0.1M $HClO_4$ and corrected for the background current. The background current was obtained by saturating the 0.1M KOH electrolyte in $N_2$ gas and obtaining a linear sweep scan. Additionally, the ORR performance in aprotic solutions is carried out in an air-sealed three-necked flask using a solution of $LiPF_6$ in tetraethylene glycol dimethyl ether (TEGDME) as the aprotic electrolyte and Li metal as the counter and reference electrode to investigate the capabilities of the catalyst for Li-$O_2$ applications. The results are also corrected for the background current by obtaining a linear sweep scan of the FePAN nnaofibrous catalyst in Ar-saturated TEGDME electrolyte.

In this case, PAN was chosen as the carbon material as it also contains nitrogen. Furthermore, PAN has long been used as a material in forming highly conductive carbon

nanofibers,[93,94] thus resulting in the facile formation of nanofibrous catalysts. Morphology of the FePAN nanofibrous catalyst was analyzed via SEM and TEM imaging. TEM samples were prepared by dispersing the catalyst in methanol before applying a droplet of the dispersed catalyst onto a copper grid. The surface areas of the FePAN nanofibrous catalysts are determined via BET analysis. Samples were degassed at a temperature of 250 °C for 12 h before obtaining the Nitrogen adsorption isotherm. XPS analysis was conducted on the N 1s, C 1s, and Fe 2p lines for the catalyst at a take-off angle of 90° using an Al Kα X-ray source with a spot area of 400 μm.

### 4.2.3 Resuts and discussion

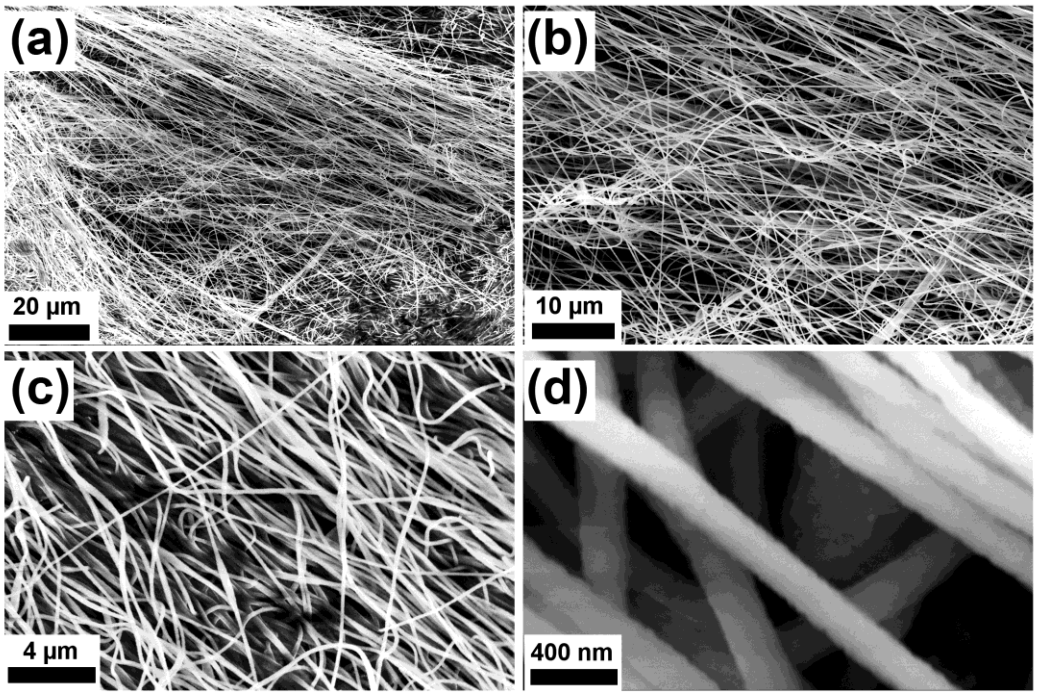


**Figure 4.12.** Electrospun Fe/PAN nanofibers various magnifications.

The electrospun PAN nanofibers containing iron acetate are shown in Figure 4.12. The nanofibers are arranged in a mesh with diameters of 100-200 nm. The nanofibers retain their

diameter after pre-oxidation and carbonization. From Figure 4.13, it is possible to see that the pyrolyzed iron containing FePAN nanofibrous catalysts remain in a mesh with ample space between each fiber, allowing for excellent mass transport properties. The SEM images also indicate the presence of small iron particles both at the surface and embedded within the carbon nanofibers. TEM images in Figure 4.14a and 4.14c shows the rough surface morphology of the nanofibers after the first pyrolysis (FePAN-PL). The same images confirm the presence of iron particles, roughly 20 nm, in diameter, that are on the surface and embedded within a layer of carbon.

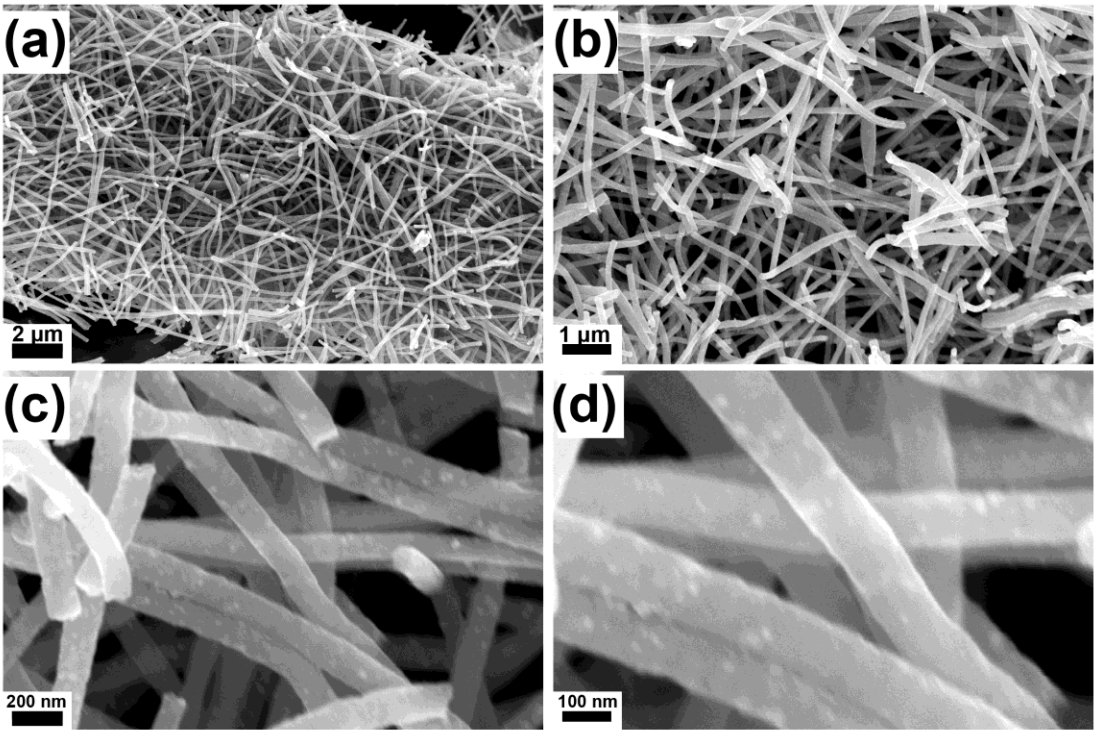


**Figure 4.13.** Electrospun Fe/PAN nanofibers various magnifications after high temperature pyrolysis in Ar gas.

Furthermore, the surface roughness of the nanofibers near the iron particles hints that the fibers may contain a porous structure after the high temperature treatment. It is possible that the iron

metal could catalyze carbonization of the fibers, causing localized weight loss, and the resulting rapid release of gaseous species[95] would result in the creation of porous carbon nanofibers. A second pyrolysis after treating the fibers in 0.5 M $H_2SO_4$ at 80 °C resulted in much rougher surfaces as seen in Figures 4.14b and 4.14c (FePAN). It is also possible to see the emergence of many more iron particles on the surface of the fibers, likely due to additional weight loss of the carbon material during the second pyrolysis. The surface roughness and empty carbon shell-like structures seen on the surface of the nanofibers further suggest that the acid leached catalyst is porous. As the surface area of the fibers directly impacts both the ORR kinetics (through mass transport), the production of porous nanofibers is an added benefit as it allows for more exposed ORR active sites as well as surface carbon sites for the formation of the discharge reaction products.

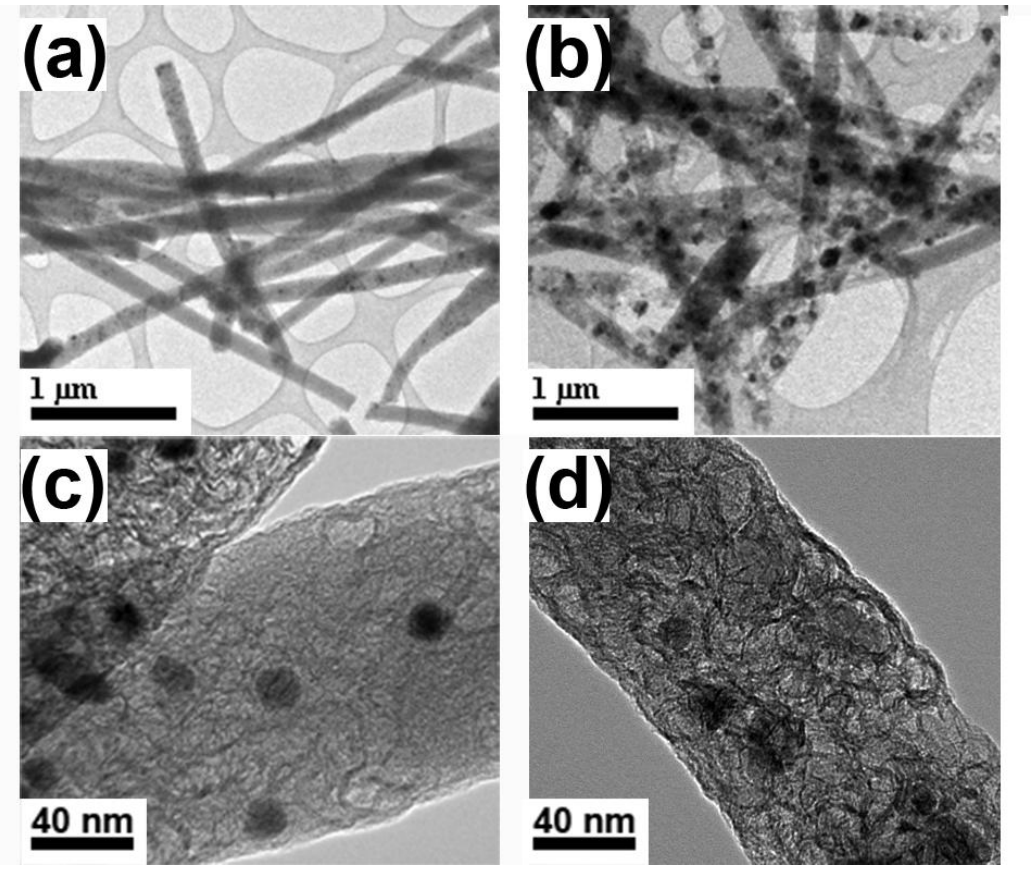


**Figure 4.14.** TEM imaging of electrospun Fe/PAN nanofibers various magnifications after high temperature pyrolysis in Ar gas before (a, c) and after (b, d) acid leaching and second pyrolysis.

To confirm the surface areas of the two samples, the BET surface areas were obtained from their respective nitrogen adsorption isotherms. A significant increase in surface area from 82.4447 $m^2$ $g^{-1}$ to 339.1079 $m^2$ $g^{-1}$, is found after acid leeching and re-pryolysis of the fibers. The result suggests that the acid leeched and re-pyrolyzed fibers should provide improved ORR performance in aqueous (alkaline and acid) and aprotic conditions.

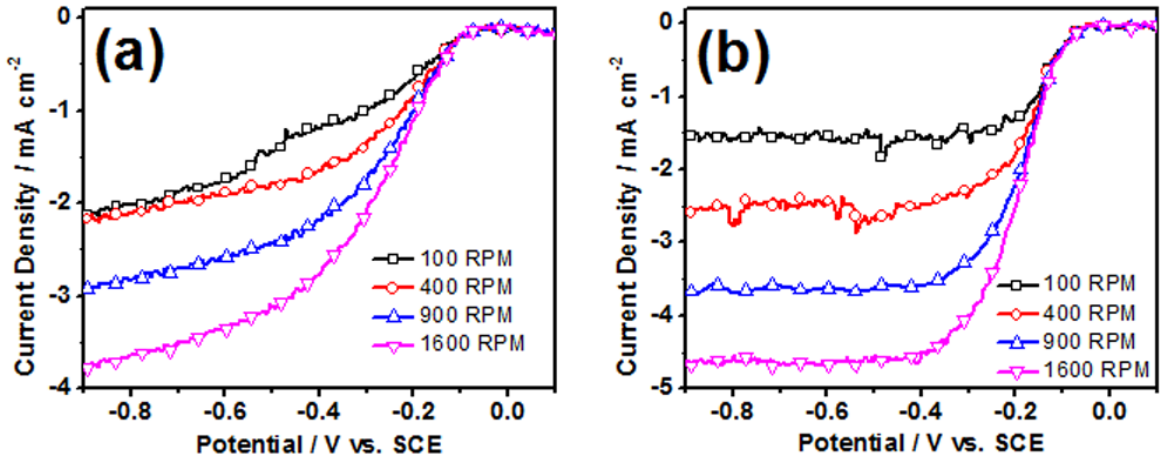


**Figure 4.15.** Half-cell ORR polarization curves of (a) FePAN-PL and (b) FePAN in $O_2$ saturated 0.1M KOH.

The half-cell ORR performance of the single pyrolyzed, pre-acid leached (FePAN-PL) and double pyrolyzed (FePAN) iron-carbon nanofibrous catalysts are shown in Figure 4.15. The benefits of higher surface area and porosity are immediately seen as the double pyrolyzed catalyst exhibits dramatically increased current densities over its single pyrolyzed predecessor. Without acid treatment and a second pyrolysis, the FePAN nanofibrous catalyst exhibits lower limiting currents and poor limiting current characteristics. After acid treatment and subsequent second pryolysis, the FePAN nanofibrous catalyst exhibits a high limiting current that plateaus quickly. The on-set potentials of both FePAN nanofibrous catalysts remain the same, suggesting that the type of active site formed during pyrolysis of the catalysts is not changed after acid treatment and a second pyrolysis. In this case, the acid treatment and second pyrolysis of the samples is a purely physical modification of the catalyst, and does not alter the active sites. This assumption is supported by the examination of the electronic structure of the elements of the two catalysts. A comparison of the N 1s XPS spectra, often associated with discussions of the ORR active site, can be seen in Figure 4.16a and 4.16b, for FePAN-PL and FePAN, respectively. No

difference in the two spectra can be observed with both catalysts containing the majority of the surface nitrogen in the pyridinic (398.08 eV) and graphitic (400.88 eV)[45,54,90] binding state. An analysis of the Fe 2p, C 1s, and O 1s spectra with fitted peaks are also shown in Figure 4.16. The Fe 2p spectra (Figure 4.16c and 4.16d), also show no differences in the electronic structure of iron within the two catalysts. Additionally, the Fe 2p spectra indicate that the majority of the surface iron within the two catalysts exists in an ionic state.[45,90] It is possible that the surface iron could exist as oxidized iron, nitrogen bound iron, or hydroxide bound iron. The C 1s spectra of the two catalysts exhibit large peaks at 284.8 eV, indicating that the catalysts contain large quantities of sp2-hybridized carbon,[45] followed by the next highest peaks at 285.7 eV, indicating nitrogen-carbon binding types.[45]

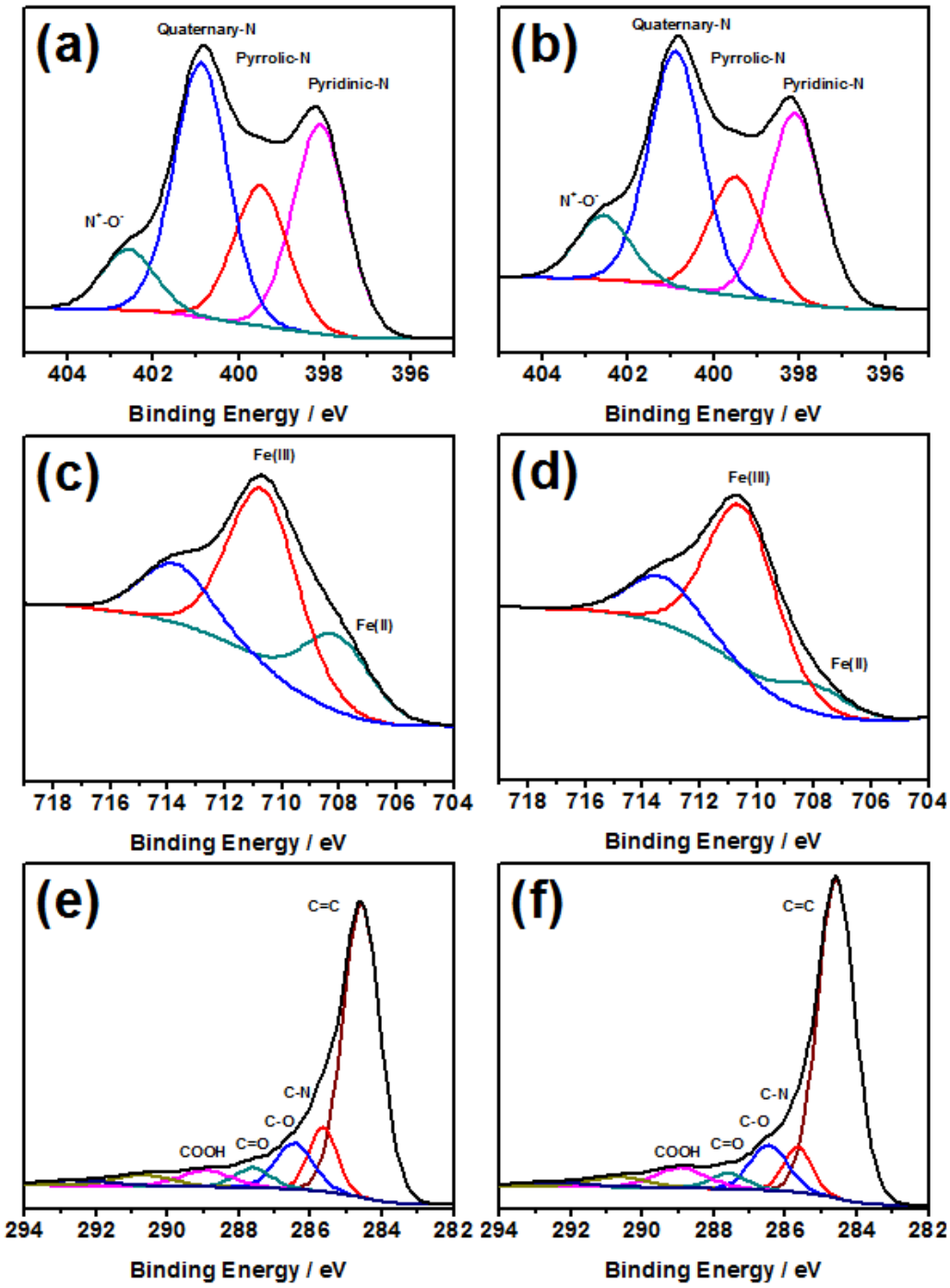


**Figure 4.16.** N 1s, Fe2p and C 1s XPS spectra of both FePAN-PL (a, c, e) and FePAN (b, d, f) nanofibrous catalysts.

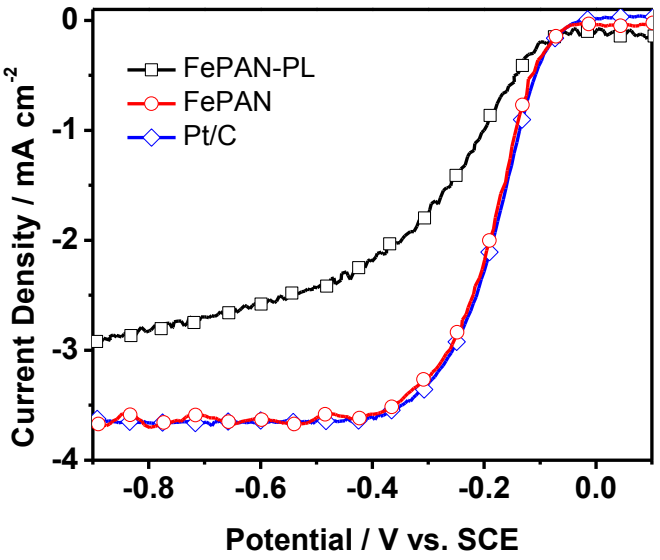


**Figure 4.17.** Comparison of ORR activity between synthesized FePAN nanofibrous catalys and commercially available Pt/C catalyst.

The high ORR activity of the FePAN nanofibrous catalyst in an aqueous alkaline environment is confirmed by comparing its performance to a commercially available Pt/C catalyst (Figure 4.17). In comparison with Pt in an aqueous environment it can be seen that the ORR activity, on-set and limiting currents, are comparable. The limiting current achieved by the non-precious FePAN nanofibrous catalyst is on par with that of the precious metal, thus significant reduction in catalyst cost can be achieved by employing non-precious catalysts without performance loss. With this in mind, it is possible to utilize non-precious carbon catalysts exhibiting superior ORR kinetics without the need to employ expensive Pt catalysts. The catalyst has an added benefit for Li-$O_2$ applications as, since the ORR catalyst is carbon based, no additional carbon support is required for the formation of lithium peroxide.

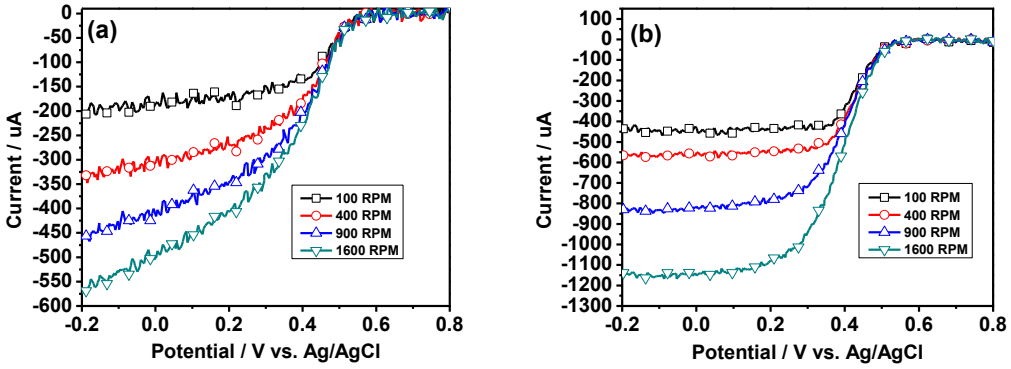


**Figure 4.18.** Half-cell ORR polarization curves of (a) FePAN-PL and (b) FePAN in $O_2$ saturated 0.1M $HClO_4$.

In addition to evaluating the FePAN nanofibrous catalyst in aqueous alkaline conditions, the nanofibrous catalyst was also evaluated for its activity in acidic conditions for PEM fuel cell applications. Much like its alkaline results, the nanofibrous catalyst exhibited very poor performance prior to acid treatment and a second pyrolysis. The result shown in Figure 4.18, shows that significant improvements in the limiting current and the behavior of the polarization curve was obtained after acid treatment and a second pyrolysis. However, the FePAN catalyst still falls behind commercial platinum based catalysts in acidic conditions, with a difference of approximately 150 mV in the half-wave potential.

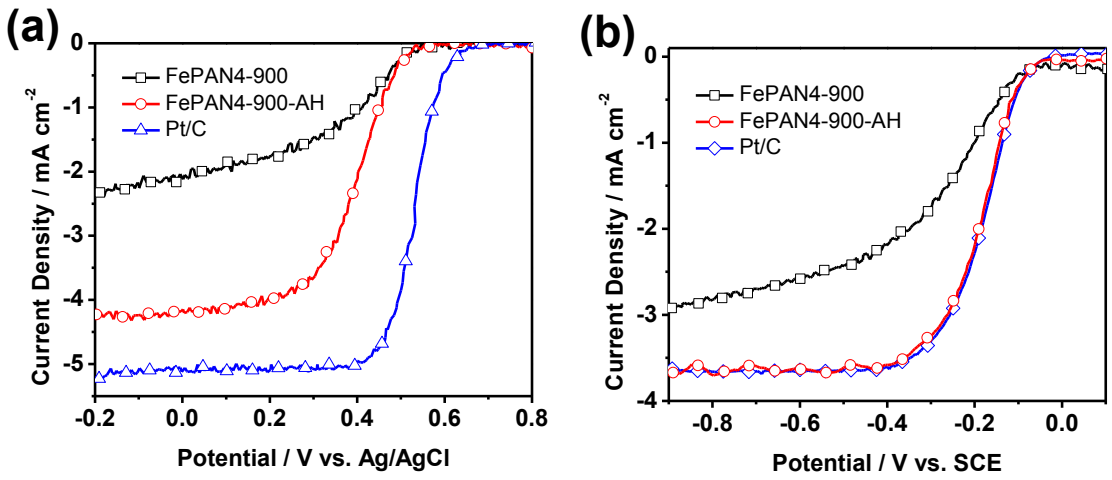


Figure **Figure 4.19.** Comparison of ORR activity between synthesized FePAN nanofibrous catalys and commercially available Pt/C catalyst in $O_2$-saturated (a) 0.1M $HClO_4$ and (b) 0.1M KOH.

The Li-$O_2$ cell performance of the non-precious FePAN nanofibrous catalyst in aprotic solutions is shown in Figure 4.20.

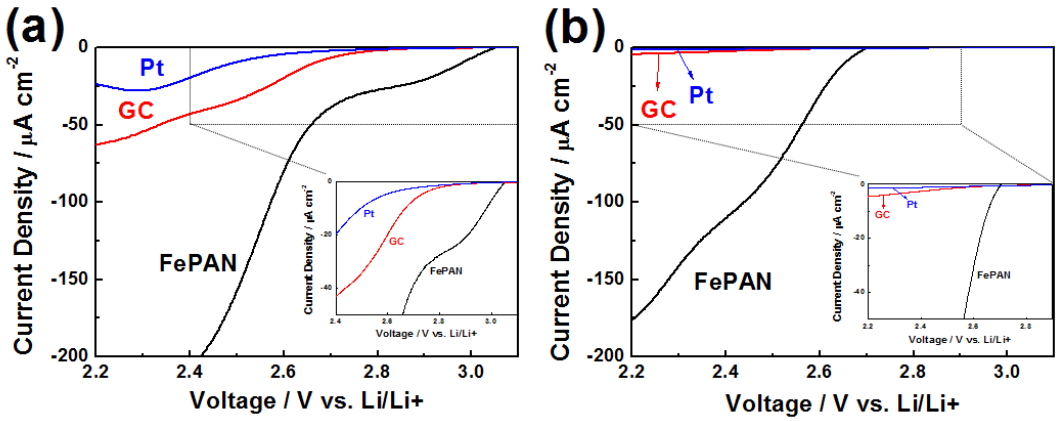


**Figure 4.20.** (a) Initial ORR polarization curves of FePAN nnaofibrous catalyst on GC, polycrystalline GC and Pt surfaces in O2-saturated 1.0 M LiPF6 in TEGDME at 900 rpm and 5 mV s-1 and (b) 5th ORR polarization curves during cycling between 2.0 V and 4.3 V.

The aprotic solution is $O_2$-saturated and the glassy carbon electrode coated with the catalyst ink is scanned from 2.0 to 4.3 V vs. Li/Li+ at a scan rate of 5 mV $s^{-1}$. The FePAN nanofibrous catalyst-coated electrode is then compared with a bare glassy carbon electrode and a Pt disk electrode. Figure 4.21 shows the cyclic voltammogram of the FePAN nanofibrous catalyst in both Ar- and $O_2$- saturated electrolytes. From the scan, it is possible to see that no electrochemical reactions are taking place without the presence of oxygen, indicating that the catalyst does not react with the aprotic electrolyte.[96]

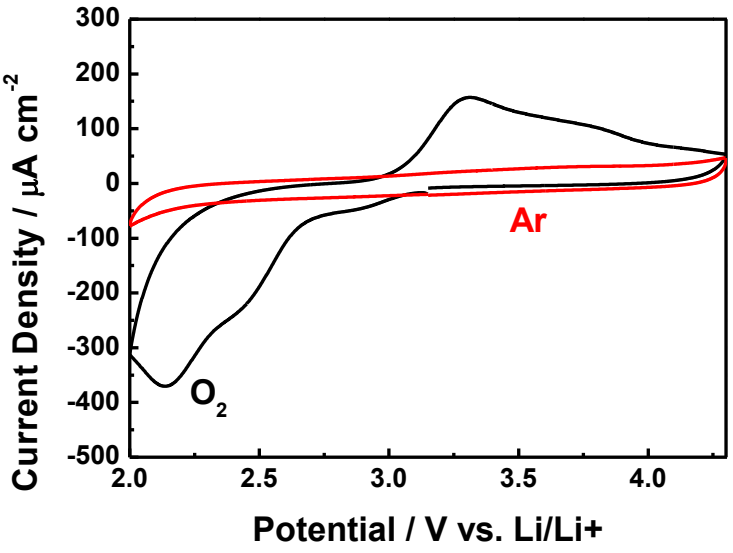


**Figure 4.21.** Cyclic voltammogram of FePAN nanofibrous catalyst in Ar- and O2-saturated TEGDME electrolyte.

The standard potential for the ORR/OER reactions are known to occur at 2.96 V vs. Li/Li+ for a two electron process, resulting in the formation of lithium peroxide ($2Li + O_2 \rightarrow Li_2O_2$) for the ORR, and the formation of lithium ions and oxygen ($Li_2O_2 \rightarrow 2Li + O_2$) for the OER. Both the

ORR and OER processes are shown to occur in the $O_2$-saturated curve in Figure 4.21 for the FePAN nanofibrous catalyst. In Figure 4.21, anodic peaks in the $O_2$-saturated curve are observed, indicating the formation of the discharge products when in the presence of oxygen (ORR). Once the reversed potential scan approaches roughly 3.3 V vs. Li/Li+, cathodic peaks are also observed, indicating the decomposition of the discharge products on the surface of the electrode (OER).[96] The FePAN nanofibrous catalyst exhibits higher reduction currents and on-set potentials than both the glassy carbon and Pt disk electrode at all potentials. The superior reduction currents achieved by the catalyst are likely due to the catalyst's significantly higher surface area as a result of the porous network of carbon fibers, allowing for more discharge reaction products to be formed.[97] The reduction on-set potential occurs at a potential closer to 2.96 V vs. Li/Li+, for the first cycle, than the on-set potentials of both Pt (2.80 V vs. Li/Li+) and the glassy carbon electrode (2.78 V vs. Li/Li+), suggesting superior ORR kinetics. Figure 4.20b shows the fifth ORR profile during cycling between 2.0 V and 4.3 V, where the FePAN nanofibrous catalyst is observed to retain acceptable current density for ORR after multiple charge-discharge cycles. The FePAN nanofibrous catalyst exhibits a maximum current density, occurring at 2.15 V vs. Li/Li+, of ca. 320 $\mu A\ cm^{-2}$ on the first cycle. The maximum current density achieved by the FePAN nanofibrous catalyst is eleven times greater than the current achieved by the Pt disk electrode (ca. 28 $\mu A\ cm^{-2}$) and five times greater than the current achieved by the glassy carbon electrode (ca. 64 $\mu A\ cm^{-2}$). On the fifth cycle, the catalyst retains 56% of the maximum current density achieved on the first cycle (ca. 180 $\mu A\ cm^{-2}$), also occurring at a potential of 2.15 V vs. Li/Li+. Both the Pt disk and glassy carbon electrode exhibit significantly lower retention of their activity after the fifth cycle. The Pt disk electrode retains only 7% of its maximum current density (ca. 28 $\mu A\ cm^{-2}$ to 2 $\mu A\ cm^{-2}$ in five cycles), and

the glassy carbon electrode retains only 9% of its maximum current density (ca. 64 μA $cm^{-2}$ to 6 μA $cm^{-2}$). The significant difference in activity retention between the FePAN nanofibrous catalyst and the two electrodes could suggest that the non-precious FePAN nanofibrous catalyst has an additional propensity towards catalyzing OER, resulting in the regeneration of active sites. Further studies and improvements to the OER activity of the catalyst as well as improving the surface area of the FePAN nanofibrous catalyst can potentially yield much higher reduction currents and cycle stability.

### 4.2.4 Summary

The use of electrospinning to produce highly active catalysts was shown in the work presented and electrospinning remains an attractive option in producing nanofibrous materials. Additionally, it was learned that significant improvement in the catalytic activity of these catalysts can be made by improving the porosity and surface area of the fibers. This was indicated by examining the effects of the acid treatment. Acid treated catalysts displayed significantly higher activities. Similar on-set potentials and XPS spectra indicate that the active sites between catalysts remain largely the same, and the improvement is likely due to a change in the physical structure of the catalyst. Indeed, TEM micrographs showing increased roughness of the surface of the catalysts also support this claim. Further experimentation involving electrospinning is intended as electrospinning can produce a mat of aligned fibers as well, thus allowing for direct spinning of a catalyst onto a gas diffusion layer of a fuel cell and allowing for the study of the effects of the arrangement of fibrous catalysts.

## 4.3 Effect of introducing sacrificial silica to electrospun Iron-polyacrylonitrile nanofibers as non-precious ORR catalysts

### 4.3.1 Introduction

Carbon nanofibers exhibit excellent properties ideal for use as catalysts. The one-dimensional structure contains lower surface energy, allowing for more stable structures. Furthermore, these supportless catalysts can be arranged into a porous mesh, allowing for efficient transport of reactants and products in the assembly. Our previous works involving catalytically active ORR carbon nanofibers has shown great promise as a non-precious metal catalyst. Polyacrylonitrile based nanofibers were synthesized as electrocatalysts via electrospinning and high temperature pyrolysis in an inert atmosphere. Previous results indicate that the catalytic activity of the nanofibrous catalysts can be significantly improved by increasing physical structure of the catalyst, such as porosity and surface area.[98,99] In this case, it may be possible to dramatically increase the activity of the catalysts further by synthesizing highly porous and high surface area PAN fibers.

Introducing sacrificial silica into the system and removing the silica particles after pyrolysis is an easy way to create voids and increase both the porosity and the surface area of the fibers. This hard-templating approach can be done using either ordered mesoporous[71,73] or amorphous silica.[70,72,75,76] For our approach, we synthesized porous fibers by introducing amorphous fumed silica into the electrospinning solution, creating a colloidal system. The solution is electrospun and the fibers, now embedded with silica particles, are pyrolyzed in an

inert atmosphere. The silica particles are then removed after pyrolysis by treating the carbonized fibers over many days. A schematic of the process is shown in the figure below.

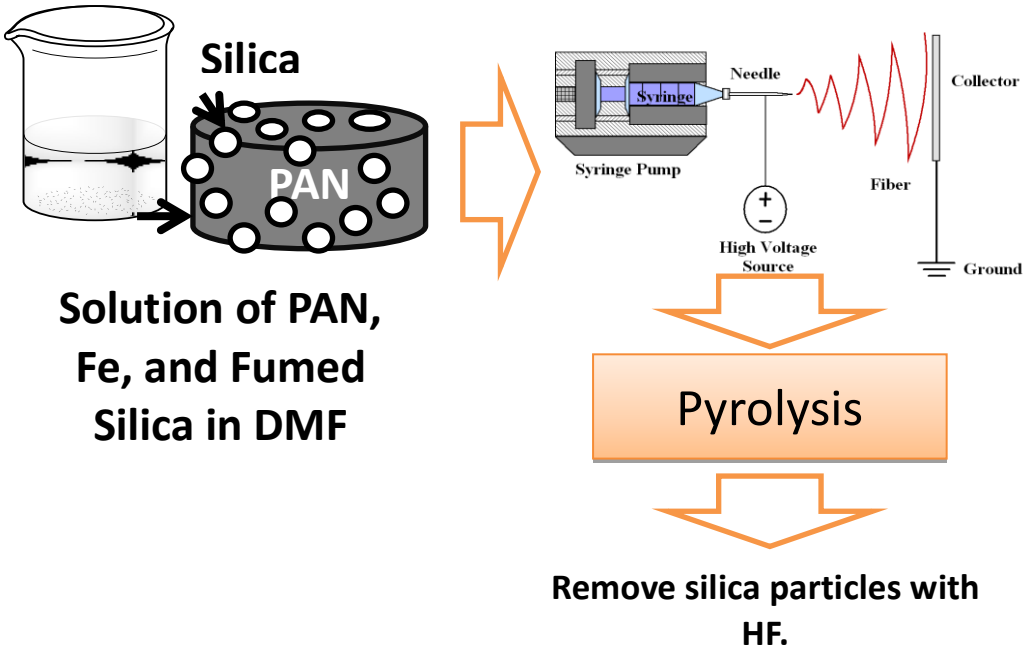


**Figure 4.22.** Schematic of the method in producing highly porous silica particles.

The resulting porous nanofibers are then characterized by SEM, BET analysis, XPS and evaluated for their ORR activity. Non-precious nanofibrous catalysts synthesized this way exhibited well behaving polarization curves with high limiting currents and positive half-wave potentials. As with the previous study, the on-set potential in region I of the polarization curve changed very little.

### 4.3.2 Experimental

Porous carbon nanofiber catalysts were synthesized via electrospinning a solution containing polyacrylonitrile, iron (II) acetate and fumed silica. First, 180 mg of polyacrylonitrile was dissolved in 3 mL of DMF after stirring and heating at 80 °C. Iron (II) acetate is then added into the solution and stirred. 43 mg of iron (II) acetate is added for 8 wt % iron catalysts, and 26.5 mg of iron (II) acetate is added for 4 wt % iron catalysts. Once both polyacrylonitrile and the iron salt have completed mixed and dissolved in DMF, fumed silica (10 nm) is added into the mixture to create an emulsion. The solution is then ultra-sonicated over night before eelctrospinning. 180 mg, 100 mg, and 50 mg of fumed silica were added for FePAN8-1, FePAN8-1.8 and FePAN8-3.6 carbon nanofiber catalysts, respectively.

Electrospinning is conducted at 10 cm from the needle tip to a grounded collector. A syringe pump is used to gradually pump at 0.008 mL/min. An electric potential of 15 kV was applied, resulting in an electric field of 150 kV/m.

The electrospun fibers were then pre-oxidized in air at 200 °C for 5 min at a heating rate of 5 °C/min before pyrolysis in an inert atmosphere at 900 °C for 30 min at a heating rate of 5 °C/min to produce ORR active carbon nanofiber catalysts. Fumed silica particles were removed by HF acid treatment for 24 h with concentrated HF acid.

ORR polarization curves were obtained in a half-cell setup using a platinum counter electrode, a reversible hydrogen electrode as the reference electrode, and a glassy carbon electrode as the working electrode. A catalyst ink consisting of 0.5 wt % nafion, ethanol, and the carbon nanofibers was applied to a glassy carbon working electrode. Results were obtained in $O_2$ saturated 0.1 M $HClO_4$ for ORR and $N_2$ saturated conditions to obtain the background current.

### 4.3.3 Results and discussion

A solution of PAN and Fe (II) Acetate was first prepared in DMF, yielding a transparent red solution after PAN and Fe (II) Acetate has completely dissolved. Fumed silica particles are then added into the transparent solution which after sonication overnight produces an emulsion of silica and PAN polymer. The solution is then electrospun and resulting fibers are arranged overlapping each other, forming a mat of interwoven nanofibers.

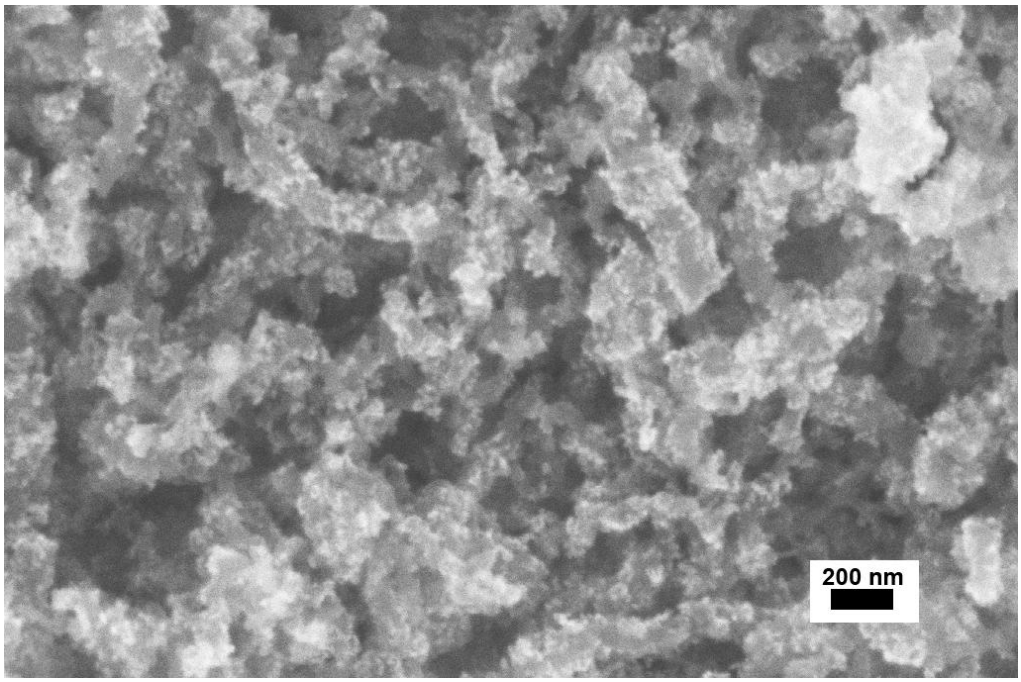


**Figure 4.23.** SEM micrograph of electrospun catalyst fibers after pyrolysis, but pre-HF treatment

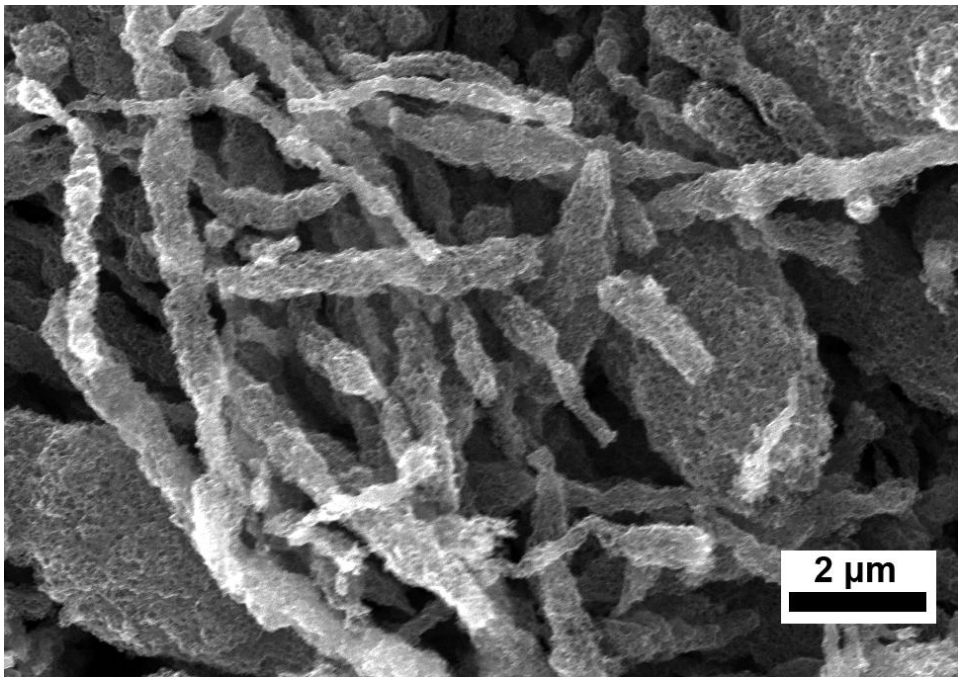


**Figure 4.24.** SEM micrograph of electrospun catalyst fibers after pyrolysis and post-HF treatment

The above Figures 4.23 and 4.24 shows the SEM micrographs of the pyrolyzed fibers before and after removal of silica using HF respectively. It is interesting to note that the introduction of sacrificial silica particles alters the morphology of the electrospun fibers. When compared to the previous study, the fibers significantly less uniform in shape and size, with many large oval-shaped modules present. It is believed that the properties of the electrospinning solution, such as surface tension and viscosity, is modified by adding fumed silica. This may cause a change in the electrospinning behaviour as electrospinning is dependent on the properties of the surface solution. The surfaces of the nanofibers are extremely rough, suggesting that the nanofibers are highly porous after removal of silica particles. BET surface area analysis of the nanoibers confirms that the nanofibers have extremely high surface area, likely due to the increased porosity introduced after removal of fumed silica particles. The BET surface areas

determined from the obtained nitrogen adsorption-desorption isotherms and total pore volume are summarized in table 4.3.

**Table 4.3-1. Summary of BET surface area and pore volume of catalysts**

| Sample | PAN:$SiO_2$ mass ratio | BET Surface Area ($m^2/g$) | Pore Volume ($cm^3/g$) |
|---|---|---|---|
| **FePAN-8%-1** | 1:1 | 607.44 | 2.49 |
| **FePAN-8%-1.8** | 1.8:1 | 483.13 | 1.12 |
| **FePAN-8%-3.6** | 3.6:1 | 359.56 | 0.46 |
| **FePAN-8%** | 0 | 82.44 | 0.14 |

From BET analysis summarized in table 4.3, it can be observed that more equivalent ratios of PAN to fumed silica produced higher surface areas and larger pore volumes. That is to say, the more fumed silica that is used, the higher the higher surface areas likely due to the voids left after removal of fumed silica particles lodged in the nanofibers.

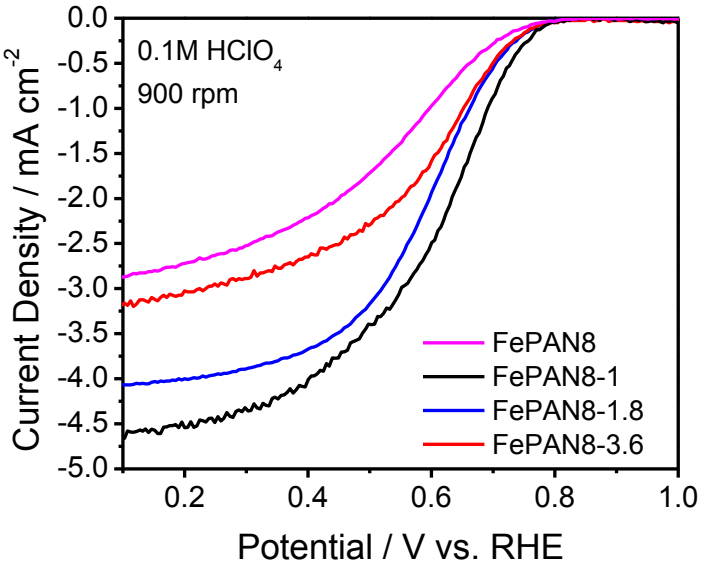


**Figure 4.25.** Comparing the ORR polarization curves of the different catalysts.

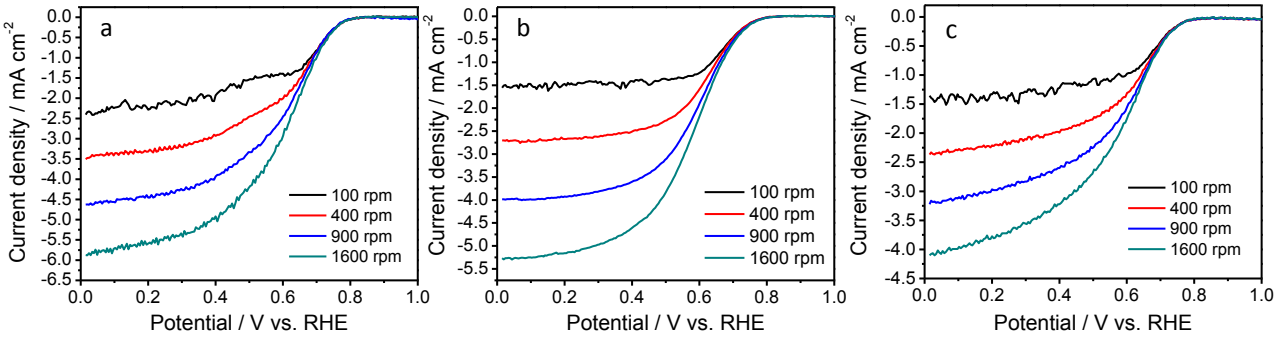


Figure 4.26. **Individual ORR polarization curves of (a) FePAN8-1, (b) FePAN8-1.8 and (c) FePAN8-3.6. All curves were obtained in 0.1M $HClO_4$ under saturated $O_2$ conditions.**

The results of more porous and higher surface area catalysts can be directly seen in figure 4.25. The individual polarization curves of the catalysts can be seen in figure 4.26. Figure 4.25 summarizes the ORR half-cell polarization curves of the carbon nanofiber catalysts. From figure 4.25, it can be seen that higher surface are catalysts directly result in an increase in the limiting current, whereas the on-set potentials of the samples remain unchanged. This is consistent in our previous work where, after acid treatment, the on-set potential also remains the same. Higher surface areas directly result in higher limiting currents. The addition of fumed silica and subsequent removal of the silica particles predominantly affects the diffusion limited and regions of the polarization curves, leaving the kinetic regions of the curves more or less static. The result suggests that the inclusion and subsequent removal of fumed silica particles affects only the physical microstructure of the carbon nanofibers, while having little to no affect on the structure or formation of active sites. XPS analyses of the samples support this claim, showing little to no change in the N 1s spectra of the catalysts.

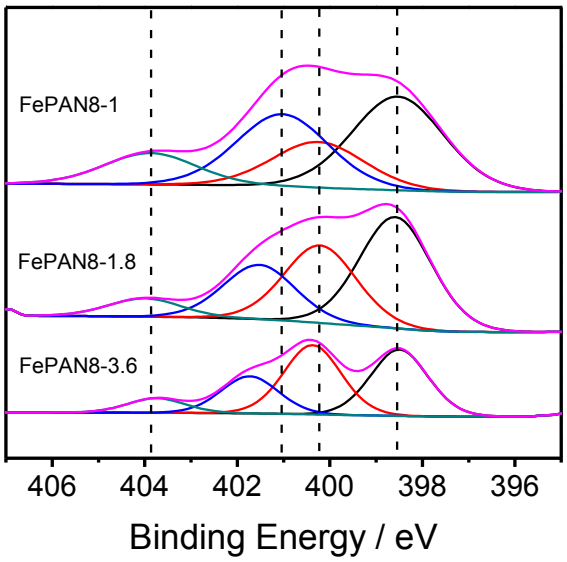


**Figure 4.27.** N 1s spectra of porous FePAN fiberous catalysts.

The N 1s spectra of the carbon nanofiber catalysts are shown in figure 4.27. Four distinct peaks at 398 eV, 400, eV, 401 eV and 402 eV can be identified, indicating presence of pyridicinic, pyrrolic, quaternary and oxidized nitrogen species respectively.[54] Pyridinic and pyrrolic nitrogen species are dominant in all samples. The C 1s spectra are shown in figure 4.28 in the supporting information. The C 1s spectra show a predominant sharp peak at 285 eV for all samples, indicating graphitization of the PAN polymer into carbonized graphitic carbon.

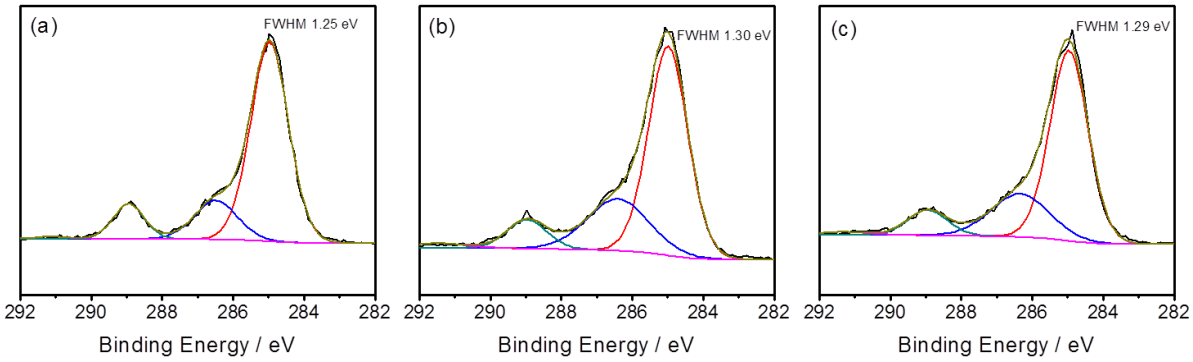


**Figure 4.28.** C 1s spectra of porous (a) FePAN8-1, (b) FePAN8-1.8, and (c) FePAN8-3.6 catalysts.

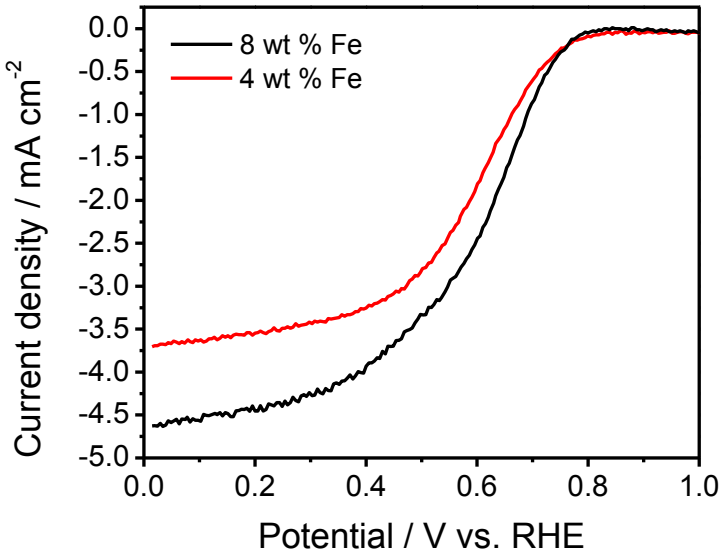


**Figure 4.29.** Comparison of ORR polarization curves of 8 wt % Fe and 4 wt % Fe for the FePAN8-1 catalyst. Curves obtained under $O_2$ saturated conditions in $HClO_4$.

Figure 4.29 shows the effects of varying iron content on the polarization curve for catalysts. Catalysts with an iron concentration of 8 wt % are more active than catalysts with 4 wt % iron. The result is consistent between catalysts synthesized with the same PAN to fumed silica ratio. The result suggests that simply increasing the surface area and porosity of catalysts is insufficient in creating more active catalysts. An optimal concentration of iron will improve

ORR activity of the catalysts, thus more active sites are formed with higher concentrations of iron. Additionally, the BET surface areas of catalysts with differing iron loadings of 4 wt % and 8 wt % remain relatively the same at 650.47 $m^2 g^{-1}$ and 607.44 $m^2 g^{-1}$ respectively. Only higher amount added of fumed silica resulted in higher surface areas, thus, at least in terms of surface area and porosity, higher loadings of iron do not affect the physical structure of the carbon nanofiber catalysts.

### 4.3.4 Summary

Highly porous carbon nanofiber catalysts were synthesized via electrospinning an emulsion of polyacrylonitrile, an iron salt, and fumed silica. After pyrolysis and subsequent removal of silica particles by HF acid treatment, the carbon nanofiber catalysts exhibited high surface area and porosity suitable to be used for catalyzing ORR. ORR polarization curves indicate higher limiting currents in samples with the highest surface areas. Reducing the iron loading in the catalysts did not affect the surface area of the carbon nanofibers, but it did result in lower activities. This result suggests that the inclusion of fumed silica particles predominantly affects the surface area and the porosity of the carbon nanofibers, allowing for efficient mass transport; however, higher loadings of iron salts are needed to produce more active catalysts.

# 5. Conclusions and Recommendations

## 5.1 Conclusions

In summary, active non-precious catalysts based on pyrolysis of carbon, nitrogen, and a transition metal were synthesized and evaluated. These non-precious catalysts exhibit high activity and consist of materials that are both abundant and cheap. Further development of these materials could bring widespread commercialization of PEM fuel cells or metal-air batteries to reality.

The first catalyst synthesized and investigated made use of a ligand containing high nitrogen content and aromatic carbons. The project explored the common techniques employed during pyrolysis of materials to produce non-precious catalysts. The nitrogen ligand, TPPQ, was synthesized and used to promote iron isolation during pyrolysis in the hopes of creating numerous, isolated active sites. It was found that more active catalysts can be achieved by employing higher loadings of iron, made possible by the structure of the ligand. However, an optimal iron loading still exists of the iron loadings investigated. Iron loadings greater than 2 wt % yielded catalysts consisting of metal iron particles which may block pores leading to catalytic active sites.

Following the work of the first project, the second project focuses on utilizing an N-containing ligand with high nitrogen content as well. In this case, polyacrylonitrile was chosen as the N-containing ligand. PAN is an excellent choice for this application as it can be used as source of both carbon and nitrogen. Furthermore PAN carbonizes into graphitic carbon at high

temperatures and is commonly used to form carbon fibers with excellent mechanical properties. A solution of PAN in DMF was prepared and electrospun to produce PAN polymer fibers in a layered, mesh-like arrangement. The polymer fibers are pre-oxidized in air and pyrolyzed along with an iron salt in an inert atmosphere, producing an ORR active catalyst. The initial ORR activity of the fibrous catalysts was not impressive; however, significant improvement in the activity was achieved after acid treatment of the catalysts. It was found that acid treatment of the catalysts changed the physical structure of the catalyst, likely increasing the porosity and surface area of the catalyst, while leaving the active sites intact. In this case, it is likely possible to synthesize highly active catalysts by simply improving the channels for which reactants can diffuse to active sites.

The third work builds upon the lessons learned from the previous project and attempts to synthesize highly active ORR catalysts by focusing on the porosity and surface area of the PAN nanofibers. In this project, sacrificial amorphous fumed silica particles were introduced into the electrospinning solution, creating a colloidal system. The colloid is then electrospun along with an iron salt and pyrolyzed the same as before. After pyrolysis, the silica particles are removed from the catalyst with HF acid. The resulting catalysts performed as expected with more porous and higher surface area catalysts exhibiting larger limiting currents and more positive half-wave potentials. The increase in porosity and surface area were both achieved by introducing more silica. Higher silica to PAN ratios resulted in higher porosities and surface areas, and consequently, more active catalysts. As with the previous study, the on-set potentials of the different catalysts remain nearly identical along with the types of nitrogen states present.

## 5.2 Recommendations

The present investigations provide an excellent basis of understanding of pyrolyzed carbon based non-precious catalysts. The studies show that it is possible to improve the activity of catalysts by focusing on the physical microstructure of the carbon. A number of future directions can be taken to gain additional insight into and improve the activity of non-precious catalysts of this type.

To a list a few directions:

1. Incorporating dopants into the carbon structure such as phosphorous could modify the electronic structure of the graphitic carbon and introduce defects into the system. Defects in particular are seen as electron withdrawing groups by the active site, and thus will help in raising the activity of the catalyst.[100]
2. Exposing the already highly porous FePAN fibrous catalysts to ammonia treatment can further increase the porosity of the carbon fibers and incorporate nitrogen into the system. Defects could also be introduced as a result.
3. The use of ordered, mesoporous silica templates or alumina templates can be experimented with to introduce interconnected pores.
4. Synthesis of hierarchal structures such as core-shell structures with a porous shell can introduce new and interesting properties to the catalyst.

# 6.0 References


(1) Bezerra, C. W. B.; Zhang, L.; Lee, K.; Liu, H.; Marques, A. a. L. B.; Marques, E. P.; Wang, H.; Zhang, J. *Electrochimica Acta* **2008**, *53*, 4937-4951.

(2) Chen, Z.; Higgins, D.; Yu, A.; Zhang, L.; Zhang, J. *Energy & Environmental Science* **2011**, *4*, 3167-3192.

(3) Mehta, V.; Cooper, J. S. *Journal of Power Sources* **2003**, *114*, 32-53.

(4) Zhang, J. *PEM Fuel Cell Electrocatalysts and Catalyst Layers*; Springer-Verlag: London, 2008.

(5) Cheng, F.; Chen, J. *Chemical Society Reviews* **2012**, *41*, 2172-2192.

(6) Lee, J.-S.; Tai Kim, S.; Cao, R.; Choi, N.-S.; Liu, M.; Lee, K. T.; Cho, J. *Advanced Energy Materials* **2011**, *1*, 34-50.

(7) Jahnke, H.; Schönborn, M.; Zimmermann, G.; Schäfer, F.; Gerischer, H.; Willig, F.; Meier, H.; Jahnke, H.; Schönborn, M.; Zimmermann, G.; Springer Berlin / Heidelberg: 1976; Vol. 61, p 133-181.

(8) Fuhrmann, A.; Wiesener, K.; Iliev, I.; Gamburzev, S.; Kaisheva, A. *Journal of Power Sources* **1981**, *6*, 69-81.

(9) Jaouen, F.; Dodelet, J. P. *Electrochimica Acta* **2007**, *52*, 5975-5984.

(10) Li, X.; Popov, B. N.; Kawahara, T.; Yanagi, H. *Journal of Power Sources* **2011**, *196*, 1717-1722.

(11) Wu, G.; More, K. L.; Johnston, C. M.; Zelenay, P. *Science* **2011**, *332*, 443-447.

(12) Alves, M. C. M.; Dodelet, J. P.; Guay, D.; Ladouceur, M.; Tourillon, G. *The Journal of Physical Chemistry* **1992**, *96*, 10898-10905.

(13) Bae, I. T.; Tryk, D. A.; Scherson, D. A. *Journal of Physical Chemistry B* **1998**, *102*, 4114-4117.

(14) Barazzouk, S.; Lefevre, M.; Dodelet, J. P. *Journal of the Electrochemical Society* **2009**, *156*, B1466-B1474.

(15) Choi, J.; Hsu, R.; Chen, Z. *The Journal of Physical Chemistry C* **2010**, *114*, 8048-8053.

(16) Chung, H. T.; Johnston, C. M.; Artyushkova, K.; Ferrandon, M.; Myers, D. J.; Zelenay, P. *Electrochemistry Communications* **2010**, *12*, 1792-1795.

(17) Lefevre, M.; Proietti, E.; Jaouen, F.; Dodelet, J.-P. *ECS Transactions* **2009**, *25*, 105-115.

(18) Lefevre, M.; Proietti, E.; Jaouen, F.; Dodelet, J. P. *Science* **2009**, *324*, 71-74.

(19) Li, S.; Zhang, L.; Liu, H. S.; Pan, M.; Zan, L.; Zhang, J. J. *Electrochimica Acta* **2010**, *55*, 4403-4411.

(20) Liu, G.; Li, X. G.; Ganesan, P.; Popov, B. N. *Electrochimica Acta* **2010**, *55*, 2853-2858.

(21) Nabae, Y.; Moriya, S.; Matsubayashi, K.; Lyth, S. M.; Malon, M.; Wu, L. B.; Islam, N. M.; Koshigoe, Y.; Kuroki, S.; Kakimoto, M. A.; Miyata, S.; Ozaki, J. *Carbon* **2010**, *48*, 2613-2624.

(22) Beck, F. *Journal of Applied Electrochemistry* **1977**, *7*, 239-245.

(23) Randin, J. P. *Electrochimica Acta* **1974**, *19*, 83.

(24) Zagal, J.; Bindra, P.; Yeager, E. *Journal of The Electrochemical Society* **1980**, *127*, 1506-1517.

(25) Zagal, J.; PÃ¡ez, M.; Tanaka, A. A.; dos Santos Jr, J. R.; Linkous, C. A. *Journal of Electroanalytical Chemistry* **1992**, *339*, 13-30.

(26) Jasinski, R. *Nature* **1964**, *201*, 1212-&.

(27) Li, W. M.; Yu, A. P.; Higgins, D. C.; Llanos, B. G.; Chen, Z. W. *Journal of the American Chemical Society* **2010**, *132*, 17056-17058.

(28) Wiesener, K. *Electrochimica Acta* **1986**, *31*, 1073-1078.

(29) Yeager, E. *Electrochimica Acta* **1984**, *29*, 1527-1537.

(30) Lee, K.; Zhang, J.; Wang, H.; Wilkinson, D. P. *Journal of Applied Electrochemistry* **2006**, *36*, 507-522.

(31) Jaouen, F.; Lefevre, M.; Dodelet, J. P.; Cai, M. *Journal of Physical Chemistry B* **2006**, *110*, 5553-5558.

(32) Vishnyakov, V. M. *Vacuum* **2006**, *80*, 1053-1065.

(33) Services, I. S. A. I. C. E. G. T. *Fuel Cell Handbook*; DOE, 2002.

(34) Larminie, J. a. D., A *Fuel Cell Systems Explained*; 2nd ed.; John Wiley & Sons Ltd.: West Sussex, 2003.

(35) Baranton, S.; Coutanceau, C.; Garnier, E.; Leger, J. M. *Journal of Electroanalytical Chemistry* **2006**, *590*, 100-110.

(36) Baranton, S.; Coutanceau, C.; Roux, C.; Hahn, F.; Leger, J. M. *Journal of Electroanalytical Chemistry* **2005**, *577*, 223-234.

(37) Ouyang, J. B.; Shigehara, K.; Yamada, A.; Anson, F. C. *Journal of Electroanalytical Chemistry* **1991**, *297*, 489-498.

(38) Shi, C.; Steiger, B.; Yuasa, M.; Anson, F. C. *Inorganic Chemistry* **1997**, *36*, 4294-4295.

(39) Shi, C. N.; Anson, F. C. *Inorganic Chemistry* **1990**, *29*, 4298-4305.

(40) van Veen, J.; Visser, C. *Electrochimica Acta* **1979**, *24*, 921-928.

(41) Wiesener, K.; Ohms, D.; Neumann, V.; Franke, R. *Materials Chemistry and Physics* **1989**, *22*, 457-475.

(42) Vasudevan, P.; Santosh; Mann, N.; Tyagi, S. *Transition Metal Chemistry (London)* **1990**, *15*, 81-90.

(43) Zagal, J. H. *Coordination Chemistry Reviews* **1992**, *119*, 89-136.

(44) Alt, H.; Binder, H.; Sandsted.G *Journal of Catalysis* **1973**, *28*, 8-19.

(45) Arechederra, R. L.; Artyushkova, K.; Atanassov, P.; Minteer, S. D. *Acs Applied Materials & Interfaces* **2010**, *2*, 3295-3302.

(46) Jaouen, F. d. r.; Herranz, J.; Lefeİ€vre, M.; Dodelet, J.-P.; Kramm, U. I.; Herrmann, I.; Bogdanoff, P.; Maruyama, J.; Nagaoka, T.; Garsuch, A.; Dahn, J. R.; Olson, T.; Pylypenko, S.; Atanassov, P.; Ustinov, E. A. *Acs Applied Materials & Interfaces* **2009**, *1*, 1623-1639.

(47) Lalande, G.; Tamizhmani, G.; Cote, R.; Dignardbailey, L.; Trudeau, M. L.; Schulz, R.; Guay, D.; Dodelet, J. P. *Journal of the Electrochemical Society* **1995**, *142*, 1162-1168.

(48) Meng, H.; Larouche, N.; Lefèvre, M.; Jaouen, F.; Stansfield, B.; Dodelet, J. *Electrochimica Acta* **2010**, *55*, 6450-6461.

(49) Lalande, G.; Faubert, G.; Cote, R.; Guay, D.; Dodelet, J. P.; Weng, L. T.; Bertrand, P. *Journal of Power Sources* **1996**, *61*, 227-237.

(50) Lefevre, M.; Dodelet, J. P.; Bertrand, P. *Journal of Physical Chemistry B* **2000**, *104*, 11238-11247.

(51) Lefevre, M.; Dodelet, J. P.; Bertrand, P. *Journal of Physical Chemistry B* **2002**, *106*, 8705-8713.

(52) Blomquist, J.; Lång, H.; Larsson, R.; Widelöv, A. *Journal of the Chemical Society, Faraday Transactions* **1992**, *88*, 2007-2011.

(53) Kramm, U.; Abs-Wurmbach, I.; Herrmann-Geppert, I.; Radnik, J.; Fiechter, S.; Bogdanoff, P. *Journal of the Electrochemical Society* **2011**, *158*, B69.

(54) Matter, P. H.; Zhang, L.; Ozkan, U. S. *Journal of Catalysis* **2006**, *239*, 83-96.

(55) Bouwkamp-Wijnoltz, A. L.; Visscher, W.; van Veen, J. A. R.; Boellaard, E.; van der Kraan, A. M.; Tang, S. C. *Journal of Physical Chemistry B* **2002**, *106*, 12993-13001.

(56) Koslowski, U. I.; Abs-Wurmbach, I.; Fiechter, S.; Bogdanoff, P. *Journal of Physical Chemistry C* **2008**, *112*, 15356-15366.

(57) Lefevre, M.; Dodelet, J. P.; Bertrand, P. *Journal of Physical Chemistry B* **2005**, *109*, 16718-16724.

(58) Weng, L. T.; Bertrand, P.; Lalande, G.; Guay, D.; Dodelet, J. P. *Applied Surface Science* **1995**, *84*, 9-21.

(59) Choi, J.-Y.; Hsu, R. S.; Chen, Z. *The Journal of Physical Chemistry C* **2010**, *114*, 8048-8053.

(60) Bambagioni, V.; Bianchini, C.; Filippi, J.; Lavacchi, A.; Oberhauser, W.; Marchionni, A.; Moneti, S.; Vizza, F.; Psaro, R.; Dal Santo, V. *Journal of Power Sources* **2011**, *196*, 2519-2529.

(61) Schulenburg, H.; Stankov, S.; Schunemann, V.; Radnik, J.; Dorbandt, I.; Fiechter, S.; Bogdanoff, P.; Tributsch, H. *Journal of Physical Chemistry B* **2003**, *107*, 9034-9041.

(62) Piela, B.; Olson, T. S.; Atanassov, P.; Zelenay, P. *Electrochimica Acta* **2009**, *55*, 7615-7621.

(63) Wu, G.; Chen, Z.; Artyushkova, K.; Garzon, F. H.; Zelenay, P. *ECS Transactions* **2008**, *16*, 159-170.

(64) Zamani, P.; Higgins, D.; Hassan, F.; Jiang, G.; Wu, J.; Abureden, S.; Chen, Z. *Electrochimica Acta* **2014**, *139*, 111-116.

(65) Chung, H. T.; Johnston, C. M.; Zelenay, P. *ECS Transactions* **2009**, *24*, 485-492.

(66) Jaouen, F.; Dodelet, J. P. *Journal of Physical Chemistry C* **2007**, *111*, 5963-5970.

(67) Koslowski, U.; Herrmann, I.; Bogdanoff, P.; Barkschat, C.; Fiechter, S.; Iwata, N.; Takahashi, H.; Nishikori, H. *ECS Transactions* **2008**, *13*, 125-141.

(68) Biddinger, E. J.; Ozkan, U. S. *Topics in Catalysis* **2007**, *46*, 339-348.

(69) Matter, P. H.; Wang, E.; Arias, M.; Biddinger, E. J.; Ozkan, U. S. *Journal of Physical Chemistry B* **2006**, *110*, 18374-18384.

(70) Serov, A.; Artyushkova, K.; Atanassov, P. *Advanced Energy Materials* **2014**, *4*, n/a-n/a.

(71) Kong, A.; Kong, Y.; Zhu, X.; Han, Z.; Shan, Y. *Carbon* **2014**, *78*, 49-59.

(72) Liang, H.-W.; Wei, W.; Wu, Z.-S.; Feng, X.; MÃ¼llen, K. *Journal of the American Chemical Society* **2013**, *135*, 16002-16005.

(73) Cheon, J. Y.; Kim, T.; Choi, Y.; Jeong, H. Y.; Kim, M. G.; Sa, Y. J.; Kim, J.; Lee, Z.; Yang, T.-H.; Kwon, K.; Terasaki, O.; Park, G.-G.; Adzic, R. R.; Joo, S. H. *Sci. Rep.* **2013**, *3*.

(74) Jiao, Y.; Zheng, Y.; Jaroniec, M.; Qiao, S. Z. *Journal of the American Chemical Society* **2014**, *136*, 4394-4403.

(75) Serov, A.; Robson, M. H.; Artyushkova, K.; Atanassov, P. *Applied Catalysis B: Environmental* **2012**, *127*, 300-306.

(76) Robson, M. H.; Serov, A.; Artyushkova, K.; Atanassov, P. *Electrochimica Acta* **2012**, *90*, 656-665.

(77) Olson, T. S.; Chapman, K.; Atanassov, P. *Journal of Power Sources* **2008**, *183*, 557-563.

(78) Qu, L.; Liu, Y.; Baek, J.-B.; Dai, L. *ACS Nano* **2010**, *4*, 1321-1326.

(79) Cote, R.; Lalande, G.; Guay, D.; Dodelet, J. P.; Denes, G. *Journal of the Electrochemical Society* **1998**, *145*, 2411-2418.

(80) Jansen, R. J. J.; Vanbekkum, H. *Carbon* **1995**, *33*, 1021-1027.

(81) Jaouen, F.; Serventi, A. M.; Lefevre, M.; Dodelet, J. P.; Bertrand, P. *Journal of Physical Chemistry C* **2007**, *111*, 5971-5976.

(82) Wang, X. Q.; Lee, J. S.; Zhu, Q.; Liu, J.; Wang, Y.; Dai, S. *Chemistry of Materials* **2010**, *22*, 2178-2180.

(83) Li, W.; Wu, J.; Higgins, D. C.; Choi, J.-Y.; Chen, Z. *ACS Catalysis* **2012**, *2*, 2761-2768.

(84) Kundu, S.; Xia, W.; Busser, W.; Becker, M.; Schmidt, D. A.; Havenith, M.; Muhler, M. *Physical Chemistry Chemical Physics* **2010**, *12*, 4351-4359.

(85) Dong, Z.; Kennedy, S. J.; Wu, Y. *Journal of Power Sources* **2011**, *196*, 4886-4904.

(86) Li, D.; Xia, Y. N. *Advanced Materials* **2004**, *16*, 1151-1170.

(87) Lalande, G.; Cote, R.; Guay, D.; Dodelet, J. P.; Weng, L. T.; Bertrand, P. *Electrochimica Acta* **1997**, *42*, 1379-1388.

(88) Moll, R. B.; Poziomek, E. J.; Mosher, W. A. *Journal of Organic Chemistry* **1971**, *36*, 1056-&.

(89) Faubert, G.; Lalande, G.; Cote, R.; Guay, D.; Dodelet, J. P.; Weng, L. T.; Bertrand, P.; Denes, G. *Electrochimica Acta* **1996**, *41*, 1689-1701.

(90) Bezerra, C. W. B.; Zhang, L.; Lee, K. C.; Liu, H. S.; Zhang, J. L.; Shi, Z.; Marques, A. L. B.; Marques, E. P.; Wu, S. H.; Zhang, J. J. *Electrochimica Acta* **2008**, *53*, 7703-7710.

(91) Faubert, G.; Cote, R.; Dodelet, J. P.; Lefevre, M.; Bertrand, P. *Electrochimica Acta* **1999**, *44*, 2589-2603.

(92) Charreteur, F.; Jaouen, F.; Ruggeri, S.; Dodelet, J. P. *Electrochimica Acta* **2008**, *53*, 2925-2938.

(93) Zhou, Z.; Lai, C.; Zhang, L.; Qian, Y.; Hou, H.; Reneker, D. H.; Fong, H. *Polymer* **2009**, *50*, 2999-3006.

(94) Sedghi, A.; Farsani, R. E.; Shokuhfar, A. *Journal of Materials Processing Technology* **2008**, *198*, 60-67.

(95) Watanabe, T.; Ohtsuka, Y.; Nishiyama, Y. *Carbon* **1994**, *32*, 329-334.

(96) Laoire, C. O.; Mukerjee, S.; Plichta, E. J.; Hendrickson, M. A.; Abraham, K. M. *Journal of The Electrochemical Society* **2011**, *158*, A302-A308.

(97) Girishkumar, G.; McCloskey, B.; Luntz, A. C.; Swanson, S.; Wilcke, W. *The Journal of Physical Chemistry Letters* **2010**, *1*, 2193-2203.

(98) Wu, J.; Park, H. W.; Yu, A.; Higgins, D.; Chen, Z. *The Journal of Physical Chemistry C* **2012**, *116*, 9427-9432.

(99) Wu, J.; Higgins, D. C.; Chen, Z. *ECS Transactions* **2013**, *50*, 1807-1814.

(100) Ramaswamy, N.; Tylus, U.; Jia, Q.; Mukerjee, S. *Journal of the American Chemical Society* **2013**, *135*, 15443-15449.